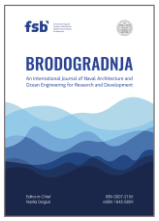
Brodogradnja Volume 78 Number 1 (2027) 78105

University of Zagreb
Faculty of Mechanical
Engineering and Naval
Architecture

journal homepage: www.brodogradnja.fsb.hr

Brodogradnja

An International Journal of Naval Architecture and
Ocean Engineering for Research and Development



# Dynamic gas-electric energy network construction and joint economic low-carbon dispatch optimization for hybrid ships

*Zhongbo Tang*[1], *Jundong Zhang*[1,2*], *Jiale Li*[1], *Fangting He*[1], *Pengzhi Liao*[1]

[1]*Marine Engineering College, Dalian Maritime University, Dalian 116026, China*
[2] *Dalian Maritime University Smart Ship Limited Company, Dalian 116026, China*

**ARTICLE INFO**

Hybrid power ship
Gas-electric coupling system
Dynamic gas network
Time-frequency domain transformation
Economic low-carbon dispatch

**ABSTRACT**

To address the time-scale mismatch between gas network dynamics (minutes to hours) and power grid response (milliseconds) in hybrid ships, which renders steady-state gas network models overly conservative under propulsion load fluctuations and limits gas-fired unit output, this paper proposes a dynamic gas network model via time-frequency transformation and a joint economic low-carbon dispatch framework. First, gas pipeline PDEs are reduced to frequency-domain algebraic equations, forming a dynamic circuit model with gas resistance, inductance, capacitance, and pressure sources. On a 4-node network, the method achieves a computational speedup of 4.6× over FDM (9.89 s) and 3.7× over FEM (7.9 s), with a runtime of 2.14 s (8 iterations) and mean absolute errors of $10^{-4}$, enabling fast dynamic power flow calculation. Second, the ε-constraint method solves the economic-carbon Pareto front, and a gas-electric closed-loop tightening mechanism yields a two-stage "rigid constraint-flexible regulation" strategy. Results show that applying dynamic constraints reduces gas-fired output by 6.7 % while increasing diesel output by 8.2-10.9 %, cutting total cost by 0.4 % at the expense of a 1.65 % emission increase - reflecting the inherent economic-environmental trade-off. Compared with the steady-state model, the dynamic model increases gas-fired generation share by 3.89 %, lowers cost by 0.13%, cuts emissions by 1.59 %, reduces gas-fired power fluctuation by 13.6-19.8 %, and decreases node pressure and flow fluctuations by approximately 72 % and 19-26 %, respectively, significantly enhancing operational stability and safety. The computation time of 55.7 s (5.65× that of the steady-state model) remains acceptable for day-ahead dispatch, and the method's robustness is confirmed by comprehensive sensitivity analyses. This work provides theoretical and technical support for economic low-carbon operation of hybrid ship gas-electric systems.

## 1. Introduction

### 1.1 Research background and significance

With growing global emphasis on environmental protection and sustainable development, the shipping industry faces urgent pressure to reduce carbon emissions and fossil fuel dependence. Stringent IMO

* Corresponding author.
E-mail address: zhjundong@dlmu.edu.cn

https://doi.org/10.21278/brod78105
Received 26 June 2026; Received in revised form 16 August 2026; Accepted 01 October 2026
Available online 03 November 2026
ISSN 0007-215X; eISSN 1845-5859

regulations have accelerated the transition to clean energy [1]. Hybrid ships, with low emissions and high efficiency, have become key alternatives to traditional vessels [2]. Recent studies have explored various hybrid marine power system configurations, including techno-economic and environmental optimization of alternative fuel pathways [3] and integrated propulsion systems for LNG carriers [4], highlighting the growing interest in gas-electric hybrid solutions for the shipping industry. Gas-electric coupling systems, as an important form of integrated ship energy systems, offer advantages in energy security, low-carbon transition, and economic operation [5]. However, a core challenge is the time-scale mismatch between gas network dynamics (minutes to hours) and power grid instantaneous response (milliseconds). Traditional studies often use steady-state gas network models, ignoring gas inertia, pressure wave propagation, and line-pack effects. While acceptable under slowly varying loads, steady-state models become overly conservative under drastic load fluctuations (e.g., sudden ship propulsion changes), limiting gas-fired unit output. Therefore, this study employs a time-frequency domain transformation to establish a dynamic gas network constraint model. Through gas-electric closed-loop coupling, coordinated optimization is achieved, and the dynamic model's advantages in economy, low-carbon performance, and stability are validated. The outcomes provide theoretical value for advancing integrated ship energy system optimization, guiding engineering practice, and promoting economic low-carbon energy transitions.

Unlike land-based gas-electric systems, shipboard natural gas networks exhibit fundamentally different dynamic characteristics due to four unique factors. First, short pipelines (30-70 m) reduce pressure wave propagation times to milliseconds or seconds, making the dynamic time constants two to three orders of magnitude smaller than those of onshore transmission networks (tens to hundreds of kilometers). This requires the dynamic model to capture transient responses at much finer time resolutions. Second, severe load shocks induced by ship maneuvering, sea states, and operational mode changes cause propulsion load fluctuations that are far more rapid and intense than typical onshore load variations, demanding faster gas network response and more frequent re-optimization. Third, the compact spatial layout of shipboard systems introduces numerous bends, fittings, and diameter changes, making local pressure losses and coupling effects among pipelines more significant than in land-based networks where frictional losses dominate. Fourth, navigation-induced rolling motion imposes additional inertial forces and alters the gas–liquid interface dynamics within pipelines, affecting gas flow characteristics in ways not present in stationary onshore systems. These factors collectively render land-based gas network models inapplicable to shipboard scenarios and necessitate the development of a dedicated dynamic gas network model tailored for hybrid ships.

### 1.2 Research status

Driven by urgent global demand for clean energy, natural gas has gained widespread attention. Research on natural gas pipeline network modeling focuses on: 1) Steady-state models: Marfatia et al. [6] improved optimization efficiency by analyzing steady-state flow properties; Ganter et al. [7] enhanced robustness under extreme conditions; Yang et al. [8] proposed a multi-port equivalent model for gas-electric coupling situational awareness. 2) Dynamic models: Farzaneh-Gord et al. [9] used analytical solutions to avoid high computational costs; Li et al. [10] developed a frequency response function (FRF)-based method for leak diagnosis; Dzedzemane et al. [11] created a state-space nonlinear model for process control; Fakhroleslam et al. [12] employed an autoregressive neural network to improve speed while maintaining accuracy. 3) Coordinated scheduling with dynamics: Gao et al. [13] used line pack to smooth renewable fluctuations; Bayani et al. [14] revealed how grid ramping affects pipeline pressure; Huang et al. [15] quantified demand uncertainty impact via electrical analogy. 4) Dynamic optimization under uncertainty: Wen et al. [16] proposed a look-ahead control strategy to enhance load response. 5) Hydrogen-enriched natural gas networks: Zhou et al. [17] simulated pressure/flow variations under different operating conditions; Zhang et al. [18] found hydrogen alters hydrodynamics, requiring compressor power optimization; Arya et al. [19] developed an ant colony optimization model for economic and environmental performance.

Joint dispatch optimization of ship multi-energy systems is a research hotspot, aiming to improve energy efficiency, reduce emissions, and enhance stability. Research focuses on energy management, optimal dispatch, and hierarchical optimization. 1) Energy management strategies: Wang et al. [20] developed a hydrogen-electric-thermal system using MILP day-ahead scheduling and MPC real-time optimization.

Liu et al. [21] proposed NMPC-based management to balance hydrogen use and stability. Zhang et al. [22] used two-layer MPC to smooth load fluctuations. Pang et al. [23] applied EKF-MPC to combine LNG engines with hybrid propulsion for fuel efficiency and CO reduction. 2) Multi-objective dispatch: Si et al. [24] used quantum computing for configuration optimization to reduce costs and emissions. Ouyang et al. [25] combined PSO, WHR, and LHS for low-carbon economic operation. Ganjian et al. [26] used genetic algorithms to balance cost and voyage time. Wang et al. [27] applied NSGA-II to reduce costs and GHG emissions. Wang et al. [28] proposed an improved differential mutation Aquila optimizer-based dispatch strategy with waste heat recovery for hybrid ships. Lu et al. [29] proposed multi-objective collaborative optimization methods combining NSGA-II and TOPSIS, while comprehensive evaluation tools for merchant ship energy efficiency have been proposed to support operational decision-making [30]. 3) Hierarchical optimization: Najjaran et al. [31] proposed a nested method for high-speed passenger ships. Yang et al. [32] developed two-stage energy management considering battery dynamics. Wang et al. [33] used a two-layer model with electricity-gas-heat coupling. Ren et al. [34] proposed hierarchical control for propulsion systems under load fluctuations. 4) Rotation rule control: Liao et al. [35] studied a diesel-electric rotation strategy to reduce fuel consumption and extend equipment life.

The unified energy circuit theory provides a framework for analyzing and optimizing integrated energy systems (electricity, heat, natural gas). It integrates heterogeneous energy flows into a unified model for better understanding and control of energy conversion, transmission, and distribution. Key research includes: 1) Static security analysis: Bao et al. [36] used a unified energy circuit model to analyze electric, gas, and heating systems. 2) Optimal dispatch: Chen et al. [37] combined unified energy circuit theory with MPC for heating and gas networks. 3) Unified energy flow analysis: Sun et al. [38] proposed a method using node classification and modified Jacobian matrix; Luo et al. [39] developed a Newton-Raphson framework for steady-state combined energy flow. 4) Key node identification: Song et al. [40] identified critical nodes via comprehensive attribute analysis. 5) Energy circuit models: Liu et al. [41] proposed a unified model for steady-state electric-gas coupling; Huang et al. [42] presented a transient unified model and solution algorithm; Mi et al. [43] used energy-circuit theory for quasi-dynamic security assessment; Ou et al. [44] applied it to fuel cell air compressor systems, demonstrating enhanced transient response and pressure distribution determination.

### 1.3 Research gaps, contents and contribution

Despite significant progress in gas network simulation, energy management, multi-objective optimization, and unified energy circuit theory, the following shortcomings remain:

1. Insufficient gas network modeling: Steady-state models [6-8] neglect gas inertia, pressure wave propagation, and line-pack, causing overly conservative constraints under load fluctuations and limiting gas-fired unit output. Traditional dynamic methods [9-11] are computationally heavy; neural-network approaches [12] improve speed but lack interpretability and depend on data quality. Most coordinated scheduling studies [13-15] focus on land-based systems, with little shipboard dynamic coordination. Hydrogen-enriched network optimization [17-19] only analyzes hydraulic impacts, not integration with ship power system dispatch.

2. Insufficient joint dispatch of ship multi-energy systems: Current energy management strategies [20-23] inadequately model gas network dynamics, missing dynamic coupling with gas turbines. Multi-objective dispatch algorithms [24-30] use static/quasi-static gas models, ignoring dynamic constraints. Hierarchical strategies [31-34] focus on power allocation, lacking dynamic pressure/flow modeling. Rotation rule strategies [35] are empirical and lack closed-loop feedback with dynamic gas flow.

3. Insufficient unified energy circuit theory: Existing studies [36, 38-40] focus on steady-state analysis, with incomplete time-frequency domain dynamic modeling. Dispatch models [37] are applied mainly to land-based systems, rarely validated for ship hybrid power. Although dynamic unified models exist [41-46], they need better accuracy-efficiency trade-offs for short-pipeline, fast-dynamic ship gas networks, and key node vulnerability under dynamic disturbances remains unassessed.

Most critically, the foundational Unified Energy Path Theory [41-46] provides the mathematical framework for dynamic gas network modeling but has never been systematically adapted and validated for shipboard short-pipeline systems - where pipeline lengths are two to three orders of magnitude shorter, time

constants differ by 2-3 orders of magnitude, and frequency-domain numerical conditions (truncation order, historical window length, initial condition handling) must be entirely re-determined.

To address the gas-electric coupling system of hybrid ships, this paper focuses on three aspects:

1. Dynamic gas network modeling: A time-frequency domain dynamic model incorporating gas resistance, inductance, capacitance, and pressure sources is established. Frequency-domain algebraic equations are derived, and a base-value correction iteration method enables fast dynamic power flow calculation for short-pipeline shipboard gas networks.

2. Joint economic low-carbon dispatch model: A gas-electric coupling optimization model is developed using the $\varepsilon$-constraint method for the economic-carbon bi-objective. A gas-electric closed-loop iterative tightening mechanism forms a two-stage "rigid constraint-flexible regulation" dispatch strategy.

3. Impact analysis of dynamic constraints: The dynamic model is compared with steady-state and finite difference/element methods in a shipboard gas-electric system. Effects on unit output, node pressure/flow, system cost, and carbon emissions are quantified.

This paper bridges these gaps with three contributions:

1. Adaptation of the Unified Energy Path Theory to shipboard short-pipeline dynamics: While the core mathematical framework (transmission line analogy, π-type equivalence, node admittance matrix) builds upon Chen and Sun's Unified Energy Path Theory, we adapt this theory to shipboard systems with fundamentally different physical characteristics - pipeline lengths of 30-70 m (versus 10-100 km onshore), time constants differing by 2-3 orders of magnitude, and entirely different frequency-domain numerical requirements. We systematically re-validate the method against FDM and FEM, achieving a computational speedup of 4.6× with precision error of $\sim 10^{-4}$, overcoming the high computational cost issue of traditional dynamic models in shipboard scenarios.

2. First systematic "dynamic vs. steady-state" comparative analysis in shipboard gas-electric systems: No prior study has quantified the advantages of dynamic gas network modeling over steady-state models in the shipboard context. Our analysis reveals that the dynamic model - by capturing pipeline line-pack effects and pressure wave propagation - reduces node pressure fluctuations by ~72 %, node flow fluctuations by 19-26 %, and gas-fired unit power fluctuations by 13.6-19.8 %, while increasing gas-fired generation share by 3.89 %, reducing total operating cost by 0.13 %, and cutting carbon emissions by 1.59 %. These findings demonstrate that dynamic characteristics are not merely "constraints" but can be leveraged as operational resources.

3. Integration of dynamic gas network constraints with ship-specific economic-low-carbon dispatch: We develop a shipboard gas-electric joint economic-low-carbon dispatch model incorporating dynamic gas network constraints, featuring: (i) bi-objective Pareto frontier analysis (ε-constraint method) for economic-cost and carbon-emission trade-offs; (ii) a gas-electric closed-loop iterative tightening mechanism that bridges the gap between gas network simulation and power dispatch optimization; and (iii) explicit modeling of ship operational modes (sailing, berthing, loading/unloading) with mode-specific constraints on generator availability, minimum online units, and emission caps. This integrated framework fills a critical gap in dynamic coupling modeling for ship energy management that existing unified energy path theory applications have not addressed.

## 2. Model construction

This study focuses on a hybrid cruise ship with a power system comprising two 25 MW gas-fired generator units, four 16.8 MW diesel generator units, and two LNG tanks (422.5 $m^3$ each). The ship has four pod propellers: the front two fixed, the rear two rotatable 360°. Each pod has a 21.5 MW AC motor (total 86 MW). LNG is vaporized and pressurized to supply gas-fired units. The generated electricity combines with diesel output to form a diesel-gas turbine hybrid system, meeting propulsion and onboard electrical loads via a power distribution system (Figure 1).

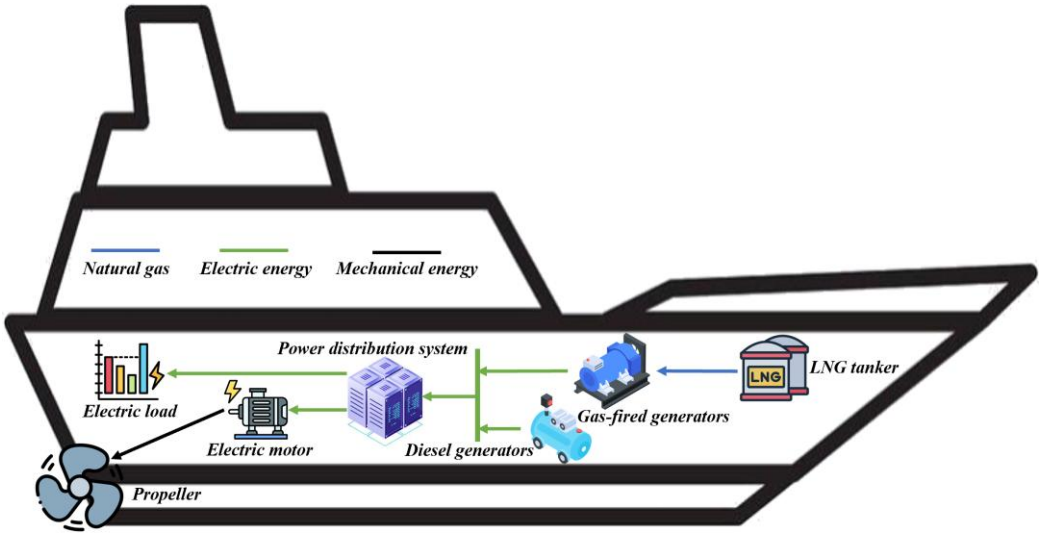



**Fig. 1** Hybrid ship structure diagram

## 2.1 Dynamic natural gas network model

### 2.1.1 Natural gas network model

This paper simplifies and models natural gas network transmission using time- and space-dependent partial differential equations. From these, gas circuit components (resistance, inductance, capacitance) are abstracted to form a distributed-parameter time-domain model. The model is then transformed to the frequency domain, converting PDEs into ordinary differential equations. Any excitation signal is decomposed into sinusoidal waves via Fourier transform, and the frequency-domain response is calculated for each frequency. By the superposition theorem, these responses are summed to obtain the total response, which is then converted back to the time domain by inverse Fourier transform.

Starting from the partial differential equation system describing the one-dimensional flow process of natural gas in pipelines, the derivation is carried out. Among them, Equation (1) reflects the material balance relationship inside the pipeline, while Equation (2) characterizes the momentum conservation property inside the pipeline:

$$\frac{\partial \rho}{\partial t} + \frac{\partial \rho v}{\partial x} = 0 \tag{1}$$

$$\frac{\partial \rho v}{\partial t} + \frac{\partial \rho v^2}{\partial x} + \frac{\partial p}{\partial x} + \frac{\lambda \rho v^2}{2D} + \rho g \sin\theta = 0 \tag{2}$$

where $\rho$, $v$ and $p$ represent natural gas density, flow rate, and pressure, respectively; $\lambda$, $D$, and $\theta$ are the friction coefficient, inner diameter, and inclination angle of the pipeline, respectively; $g$ is the acceleration due to gravity; $t$ and $x$ are the time and spatial variables in the one-dimensional flow process, respectively.

In the momentum conservation Equation (2), there are five terms: natural gas acceleration, convection, static, drag, and gravity effects. Typically, the convection and drag terms can be approximated to simplify the equation. In practical engineering, flow velocities usually do not exceed 10 m/s. When the velocity is much lower than the speed of sound, the convective term approaches zero (Equation (3)). For the drag term, incremental linearization approximates the velocity-squared term as a linear function of velocity, as shown in Equation (4):

$$\frac{\partial \rho v^2}{\partial x} \approx 0 \tag{3}$$

$$\frac{\lambda\rho v^2}{2D} = \frac{\lambda\rho(v_b + \Delta v)^2}{2D} \approx \frac{\lambda\rho(v_b^2 + 2v_b\Delta v)}{2D} = \frac{\lambda\rho(2v_b v - v_b^2)}{2D} \tag{4}$$

where $v_b$ represents the base flow rate of natural gas in the pipeline, usually taken as the flow rate under rated operating conditions; $\Delta v$ is the fluctuation amplitude of the actual flow rate of natural gas relative to the base value.

The linearization error of the drag term approximation in Equation (4) can be quantified as follows. Let $\Delta v = v - v_b$. The true drag term is $f(v) = \lambda\rho v^2/(2D)$, and its first-order Taylor approximation is $f(v) \approx (\lambda\rho/2D)(2v_b v - v_b^2)$. The truncation error is $R_2(v) = (\lambda\rho/2D)(\Delta v)^2$, giving a relative error bound:

$$\varepsilon = \left|\frac{R_2(v)}{f(v)}\right| = \frac{(\Delta v/v_b)^2}{1 + 2(\Delta v/v_b)} \tag{5}$$

This error bound is monotonically increasing with $|\Delta v|/v_b$. When $|\Delta v|/v_b \leq 20$ %, the theoretical error is below 3.33 %; when the deviation reaches 60 %, the error bound increases to 28.13 %. To mitigate this error under large velocity fluctuations, the base-value correction iteration method (Section 2.1.4) is employed. By progressively updating $v_b$ towards the actual flow velocity through multiple iterations, the relative deviation $|\Delta v|/v_b$ is progressively reduced to within 5 %, thereby limiting the actual linearization error to below 0.6 % as verified in the sensitivity analysis (Section 3.2.4). This iterative correction mechanism effectively transforms the large single-step linearization error into negligible residuals through successive refinements.

Using the gas equation of state (5) and the definition of pipeline flow rate (6), the density $\rho$ and flow velocity $v$ in the one-dimensional flow equations can be transformed into gas pressure $p$ and mass flow rate $G$:

$$p = RT\rho \tag{6}$$

$$G = \rho v A \tag{7}$$

where $R$, $T$, and $G$ are the gas constant, temperature, and mass flow rate of natural gas, respectively, and $A$ is the cross-sectional area of the pipeline.

By synthesizing Equations (1)-(7), a set of partial differential equations containing time and spatial variables can be derived to describe the relationship between flow rate and pressure during natural gas flow in pipelines：

$$A\frac{\partial p}{\partial t} + RT\frac{\partial G}{\partial x} = 0 \tag{8}$$

$$\frac{1}{A}\frac{\partial G}{\partial t} + \frac{\partial p}{\partial x} + \frac{\lambda v_b G}{AD} - \frac{\lambda v_b^2 p}{2RTD} + \frac{pg\sin\theta}{RT} = 0 \tag{9}$$

According to Equations (8) and (9), a microelement with a length of $dx$ is taken from space along the direction of the pipeline. Therefore, the airflow difference $dG$ and gas pressure difference $dp$ at both ends of this segment of pipeline microelement with a length of $dx$ can be expressed as:

$$\mathrm{d}G = -\frac{A\mathrm{d}x}{RT} \cdot \frac{\mathrm{d}p}{dt} \tag{10}$$

$$\mathrm{d}p = -\frac{\mathrm{d}x}{A} \cdot \frac{\mathrm{d}G}{\mathrm{d}t} - \frac{\lambda v_b \mathrm{d}x}{AD} \cdot G - \frac{2gD\sin\theta - \lambda v_b^2}{2RTD}\mathrm{d}x \cdot p \tag{11}$$

By analogy between gas flow, pressure, and current and voltage in the circuit, and combining Equations (10) and (11), gas path components such as gas resistance $R_g$, gas sensing $L_g$, gas capacity $C_g$ and

controlled gas pressure source $k_g$can be abstracted. The specific expressions are shown in Equations (12)-(15):

$$R_g = \frac{\lambda v_b}{AD} \tag{12}$$

$$L_g = \frac{1}{A} \tag{13}$$

$$C_g = \frac{A}{RT} \tag{14}$$

$$k_g = \frac{2gD\sin\theta - \lambda v_b^2}{2RTD} \tag{15}$$

So the entire natural gas pipeline with a length of $L$ can be represented as a distributed parameter gas path composed of multiple microelements with a length of $\mathrm{d}x$. The pipeline with a length of $\mathrm{d}x$ can be represented as a section of gas path including gas resistance $R_g$, gas sensing $L_g$, gas capacity $C_g$, and controlled gas pressure source element $k_g$, as shown in Figure 2.

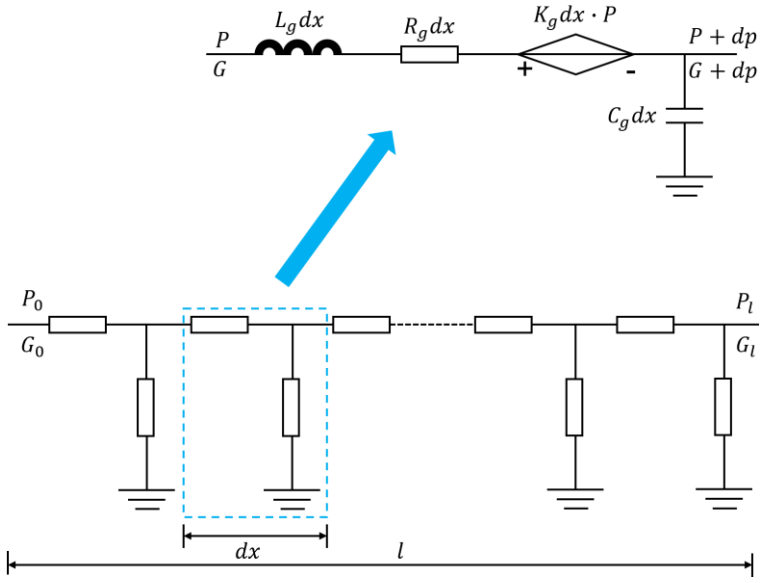



**Fig. 2** Distribution parameters of the natural gas pipeline gas path [41]

After obtaining the time-domain distribution parameters of the natural gas pipeline, the gas path Equations (9) and (10) are mapped and converted to the frequency domain to obtain the frequency-domain distribution parameters of the natural gas network equations corresponding to different frequency components. Further Fourier transform the changes in airflow and gas pressure over time, and record $\tilde{G}(x,\omega) = \mathcal{F}[G(x,t)]$, $\tilde{p}(x,\omega) = \mathcal{F}[p(x,t)]$:

$$\frac{\mathrm{d}\tilde{G}}{\mathrm{d}x} = -j\omega C_g \cdot \tilde{p} \tag{16}$$

$$\frac{\mathrm{d}\tilde{p}}{\mathrm{d}x} = -\left(R_g + j\omega L_g\right)\tilde{G} - k_g\tilde{p} \tag{17}$$

Based on the boundary conditions at the inlet of the pipeline: $\tilde{G}\big|_{x=0} = \widetilde{G_0}$ and $\tilde{p}|_{x=0} = \widetilde{p_0}$, the airflow $G_L$ and gas pressure $P_L$ at the end of the pipeline can be solved from Equations (16) and (17). In addition, the

relationship between this cascaded linear two port network can be represented by a transition matrix in Equation (18):

$$\begin{bmatrix}\widetilde{p_L}\\ \widetilde{G_L}\end{bmatrix}=\begin{bmatrix}A & B\\ C & D\end{bmatrix}\begin{bmatrix}\widetilde{p_0}\\ \widetilde{G_0}\end{bmatrix} \tag{18}$$

In the formula, $A$, $B$, $C$ and $D$ are network parameters, respectively:

$$A=\left[\cosh\left(\frac{L}{2}\sqrt{k_g^2+4\gamma_{gc}}\right)-\frac{k_g}{\sqrt{k_g^2+4\gamma_{gc}}}\cdot\sinh\left(\frac{L}{2}\sqrt{k_g^2+4\gamma_{gc}}\right)\right]\cdot \mathrm{e}^{-k_gL/2} \tag{19}$$

$$B=-\frac{2}{\sqrt{k_g^2+4/Z_{gc}}}\cdot\sinh\left(\frac{L}{2}\sqrt{k_g^2+4\gamma_{gc}}\right)\cdot \mathrm{e}^{-k_gL/2} \tag{20}$$

$$C=\left[-\frac{2}{\sqrt{k_g^2+4Z_{gc}}}\cdot\sinh\left(\frac{L}{2}\sqrt{k_g^2+4\gamma_{gc}}\right)\right]\cdot \mathrm{e}^{-k_gL/2} \tag{21}$$

$$D=\left[\cosh\left(\frac{L}{2}\sqrt{k_g^2+4\gamma_{gc}}\right)+\frac{k_g}{\sqrt{k_g^2+4\gamma_{gc}}}\cdot\sinh\left(\frac{L}{2}\sqrt{k_g^2+4\gamma_{gc}}\right)\right]\cdot \mathrm{e}^{-k_gL/2} \tag{22}$$

Note $Z_g=R_g+j\omega L_g$, $Y_g=j\omega C_g$, where $\gamma_{gc}=Z_gY_g$ and $Z_{gc}=Z_g/Y_g$ are respectively analogous to the propagation coefficient and characteristic impedance of power transmission lines. The cascaded linear two port network described by Equation (17) can be equivalent to a $\pi$-type equivalent natural gas delivery pipeline, as shown in Figure 3. The relevant parameters in the equivalent gas path can be calculated through Equations (23)-(26):

$$y_b=-1/B \tag{23}$$

$$K=1-AD+BC \tag{24}$$

$$Y_1=(AD-BC-A)/B \tag{25}$$

$$Y_2=(1-D)/B \tag{26}$$

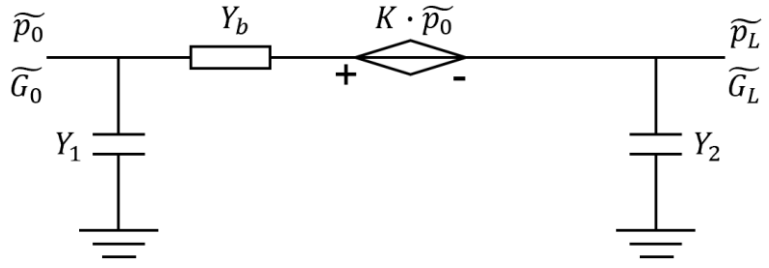



**Fig. 3** $\pi$-type equivalent gas path of the natural gas pipeline

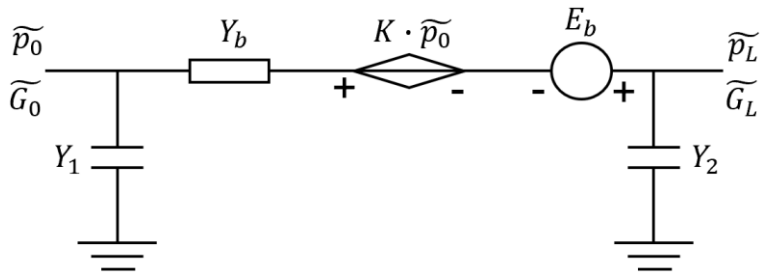



**Fig. 4** $\pi$-type equivalent gas path of the natural gas pipeline with pressure source

When a linear two port network includes a compressor or other boosting device, a pressure source $E_b$ can also be introduced, as shown in Figure 4. By using the $\pi$-type equivalent gas path model, the admittance equation of a multi-node natural gas network can be constructed.

Besides gas resistance, gas sensing, gas volume, and controlled pressure source components, there is another common component in natural gas networks that corresponds to the pressure source of the booster, modeled by Equation (27).

$$P_1 = P_2 + E_g \tag{27}$$

where $P_1$ and $P_2$ are the gas pressures on both sides of the pressure source; $E_g$ is the pressure increment provided by the pressure source.

For a general branch composed of the five types of gas path components mentioned above, as shown in Figure 5, its branch equation can be expressed as:

$$G_b = y_b(P_b + E_b - k_b P_f) \tag{28}$$

where $G_b$ represents the airflow in the branch; $P_b$ is the pressure difference at both ends of the branch; $P_f$ and $P_t$ represent the gas pressure at the beginning and end of the branch, respectively; $y_b$ is the branch admittance composed of gas resistance, gas sensing, and gas capacity; $k_b$ and $E_b$ are the component parameters of the controlled pressure source and pressure source in the branch, respectively.

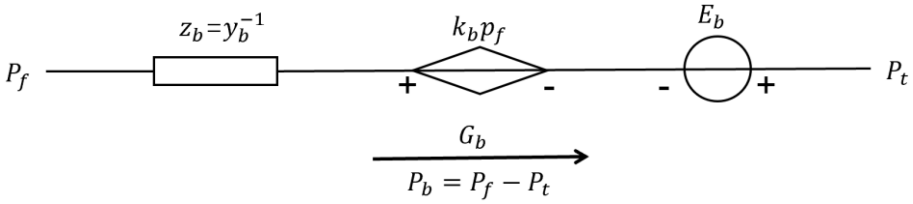



**Fig. 5** General branches in the natural gas network

Write the branch equations of all branches in the natural gas network in matrix form, as shown in Equation (29):

$$\boldsymbol{G_b} = \boldsymbol{y_b}(\boldsymbol{P_b} + \boldsymbol{E_b} - \boldsymbol{k_b}\boldsymbol{P_f}) \tag{29}$$

where $\boldsymbol{G_b}$, $\boldsymbol{P_b}$, $\boldsymbol{E_b}$, $\boldsymbol{k_b}$, and $\boldsymbol{P_f}$ are column vectors composed of corresponding branch parameters and variables; $y_b$ is a diagonal matrix composed of branch admittance.

In terms of topological constraints, the node branch correlation matrix and the node outflow branch correlation matrix are introduced to characterize the topological characteristics of natural gas networks. Record $A_g$ as the node branch correlation matrix of the natural gas network. $A_g$ is a natural gas network matrix with $n$ rows and $m$ columns, where $n$ represents the number of nodes and $m$ represents the number of branches.

Use $(A_g)_{ij}$ to represent the elements in row $i$ and column $j$. When natural gas flows out of the $j$-th branch from the $i$-th node, $(A_g)_{ij} = -1$; When natural gas flows out of the $i$-th node from the $j$-th branch,

$(A_g)_{ij}$= 1； When the $i$-th node is not connected to the $j$-th branch, $(A_g)_{ij}$= 0. Also note that $A_{g+}$ is the node outflow branch correlation matrix of the natural gas network, $A_{g-}$ is the node inflow branch correlation matrix of the natural gas network. $A_{g+}$ only retains all non-negative elements in the $A_g$ matrix, with all other elements set to zero, while $A_{g-}$ only retains all non-positive elements in the $A_g$ matrix, with all other elements set to zero.

Topological constraints in natural gas networks are mainly divided into two types: “flow” constraints and “potential” constraints. The “flow” constraint means that the natural gas flow through a node follows mass conservation: the difference between the mass flowing out and the mass flowing into the node equals the natural gas injection amount at that node:

$$A_g G_b = G_n \tag{30}$$

where $G_n$ represents the column vector formed by the injection of natural gas flow at each node.

The "potential" constraint refers to the conservative nature of natural gas pressure at each node (since pressure and gravity are determined by conservative forces). After one cycle along any closed loop, the total change in natural gas pressure should be zero, as expressed by Equation (31). The pressure at the head of the branch is determined by Equation (32).

$$A_g^T P_n = P_n \tag{31}$$

$$A_{g+}^T P_n = P_f \tag{32}$$

Branch characteristics describe the relationships between branch variables in the natural gas network, while topological constraints reflect the correlation between branch and node variables. Substituting topological constraints into the branch characteristic equation yields the unreduced form of the natural gas network Equation (33):

$$G_n = A_g y_b (A_g^T P_n + E_b - k_b A_{g+}^T P_n) \tag{33}$$

The node pressure-airflow equation can be expressed as:

$$\left(A_g Y_b A_g^T - A_g Y_b k_b A_{g+}^T + A_{g+} Y_1 A_{g+}^T + A_{g-} Y_2 A_{g-}^T\right)\widetilde{p_n} = \widetilde{G_n} - A_g Y_b E_b \tag{34}$$

where $Y_b$, $k_b$, $Y_1$, $Y_2$ and $E_b$ are diagonal matrices formed by corresponding parameters of each $\pi$-type equivalent pipeline; $\widetilde{p_n}$ and $\widetilde{G_n}$ are column vectors of node pressure and airflow in the frequency domain. Denoting $Y_g = A_g Y_b A_g^T - A_g Y_b k_b A_{g+}^T + A_{g+} Y_1 A_{g+}^T + A_{g-} Y_2 A_{g-}^T$ and $\widetilde{G_n}'(\omega) = \widetilde{G_n} - A_g Y_b E_b$, Equation (34) simplifies to:

$$Y_g \widetilde{P_n}(\omega) = \widetilde{G_n}'(\omega) \tag{35}$$

This shows that the natural gas network has a network equation analogous to the power network, with $Y_g$ corresponding to the admittance matrix.

Compared with the existing time-domain dynamic power flow solution of the unified energy circuit theory (e.g., FDM/FEM-based approaches), the proposed frequency-domain method offers two distinct advantages for shipboard applications. First, by converting PDEs into frequency-domain algebraic equations, the method achieves a computational speedup of 4.6× over FDM and 3.7× over FEM (Section 3.2.2), which is critical for the frequent re-optimization required in shipboard dispatch (15-minute intervals). Second, the frequency-domain approach naturally handles the high-frequency components of ship load fluctuations through spectral decomposition (Figure 10), whereas time-domain methods require fine spatiotemporal discretization to capture the same dynamics, leading to significantly higher computational costs. The truncation order m=100 is determined via spectral analysis to balance accuracy and efficiency. These advantages, enabled by the systematic re-calibration of frequency-domain parameters specifically for

shipboard short-pipeline systems, make the proposed method suitable for online re-dispatch optimization in hybrid ships.

### 2.1.2 Dynamic flow calculation of the natural gas network

Reference [46] proposes a dynamic load flow model for natural gas networks. For an N-node network, the equivalent gas path (Figure 4) connects two grounding branches to ship nodes, forming a complete path. Thus, an $m+1$-dimensional complex frequency-domain equation system is established, where $\boldsymbol{Y}_g^{\omega}$, $\dot{\boldsymbol{p}}_g^{\omega}$, and $\dot{\boldsymbol{G}}_g^{\omega}$ denote the -frequency components of each variable. The complex frequency-domain network Equation (36) is:

$$\boldsymbol{Y}_g^{\omega}\dot{\boldsymbol{p}}_g^{\omega} = \dot{\boldsymbol{G}}_g^{\omega} \tag{36}$$

Unlike the zero-frequency gas path equation, dynamic load flow extends network equations from real to complex (phasor) numbers, indicated by "·" above variables.

The ship's metal structure, with excellent conductivity, serves as a unified zero-potential "ground" reference. The simplification of the ship's metal structure as a unified zero-potential reference ground is justified by the continuous welded nature of the steel hull, which provides an electrically equipotential surface with negligible resistance (in the order of micro-ohms) across welded joints. To quantify the potential error introduced by insulation flanges and segmented structures, a conservative boundary simulation was conducted assuming two independent grounding regions with a 0.01 MPa deviation between their reference potentials. The results show that the maximum nodal pressure deviation between the unified-grounding assumption and the conservative two-ground case is less than 0.032 %, which is far below the typical engineering tolerance of 1-5 % for shipboard gas network dispatch problems.

Ship nodes are thus treated as special constant-pressure nodes with zero pressure, ensuring at least one constant-pressure node in the network. This keeps the node admittance matrix $\boldsymbol{Y}_g^{\omega}$ non-singular, satisfying the solvability condition. Transforming time-domain boundary conditions to the frequency domain yields:

$$\begin{cases} \dot{\boldsymbol{p}}_{g,g}^{\omega} = \left(\boldsymbol{Y}_{g,gg}^{\omega}\right)^{-1} \cdot \left(\dot{\boldsymbol{G}}_{g,g}^{\omega} - \boldsymbol{Y}_{g,gp}^{\omega}\dot{\boldsymbol{P}}_{g,p}^{\omega}\right) \\ \dot{\boldsymbol{G}}_{g,p}^{\omega} = \boldsymbol{Y}_{g,pg}^{\omega}\dot{\boldsymbol{P}}_{g,g}^{\omega} + \boldsymbol{Y}_{g,pp}^{\omega}\dot{\boldsymbol{P}}_{g,p}^{\omega} \end{cases} \tag{37}$$

Applying inverse Fourier transform, frequency-domain components revert to time-domain sinusoidal waves, whose superposition gives the dynamic load flow solution:

$$\begin{cases} p_{g,g}(t) = \sum_{\omega=0}^{m} \mathrm{Re}\left(\dot{p}_{g,g}^{\omega}\right) \cdot \cos(x_{\omega}t) - \mathrm{Im}\left(\dot{p}_{g,g}^{\omega}\right) \cdot \sin(x_{\omega}t) \\ G_{g,p}(t) = \sum_{\omega=0}^{\mathrm{m}} \mathrm{Re}\left(\dot{G}_{g,p}^{\omega}\right) \cdot \cos(x_{\omega}t) - \mathrm{Im}\left(\dot{G}_{g,p}^{\omega}\right) \cdot \sin(x_{\omega}t) \end{cases} \tag{38}$$

where Re(·) and Im(·) denote real and imaginary parts; $\mathrm{x}_{\omega}$ is the angular frequency of component $\omega$; $t$ is time; and $n+1$ is the total number of frequency components. Non-bold vector variables represent scalar elements.

Similarly, the dynamic load flow solution for branch state variables can be derived:

$$G_{gb}(t) = \sum_{\omega=0}^{m} \mathrm{Re}\left(\dot{G}_{gb}^{\omega}\right) \cdot \cos(x_{\omega}t) - \mathrm{Im}\left(\dot{G}_{gb}^{\omega}\right) \cdot \sin(x_{\omega}t) \tag{39}$$

### 2.1.3 Initial value equivalent method

Dynamic power flow equations for natural gas networks are PDEs, requiring both boundary and initial conditions. However, the discrete Fourier transform (used in unified energy circuit methods) cannot explicitly specify initial conditions because it deals with periodically extended infinite signals [45].

In practice, the initial condition at $T_0$ is determined by all prior boundary conditions. Due to dynamic attenuation, it can be approximated using historical boundary conditions from $[T_0 - T, T_1]$, where $T$ controls accuracy.

To compute dynamic flow over $[T_0, T_1]$, take boundary conditions over $[T_0 - T, T_1]$ for Fourier transform, solve frequency-domain equations, invert to time domain, and superimpose. If the computed flow

at $T_0$ matches the given initial condition, the solution over $[T_0, T_1]$ is acceptable; otherwise, increase $T$ and repeat.

This historical-boundary-condition approximation is practical: initial conditions are hard to measure accurately in gas networks, while historical data (e.g., tank supply and load consumption) are more readily available.

The selection of the historical window length $T$ follows two criteria. First, from the system dynamics perspective, $T$ should be at least five times the dominant time constant of the pipeline system to ensure that the influence of the initial condition at $T_0 - T$ decays to below 1 % at $T_0$. For shipboard short pipelines (30-70 m), the dominant time constant is approximately 7 s, giving a theoretical minimum of $T \geq 35$ s. Second, from the load characteristics perspective, $T$ should cover at least 2-3 cycles of the lowest-frequency load components to accurately capture low-frequency trends. Spectral analysis (Figure 10) shows that the lowest significant frequency corresponds to a period of approximately 6 hours, leading to $T \geq 12$ hours. Combining these criteria, $T = 12$ hours is selected as the practical window length.

The convergence of the initial-value equivalent method is verified through a window extension procedure: the window length $T$ is progressively increased until the change in the computed pressure/flow at $T_0$ falls below a threshold of 0.1 %. As demonstrated in the sensitivity analysis (Section 3.2.4, Table 7), increasing $T$ from 12 hours to 24 hours improves accuracy by less than 0.02 % while doubling the computation time, confirming that $T = 12$ hours lies in the asymptotic convergence range.

#### 2.1.4 Base value correction method

In the dynamic flow calculation of natural gas networks, the momentum conservation equation contains a nonlinear quadratic drag term. To enable frequency-domain solution, this term must be linearized via first-order Taylor expansion around a branch flow base value (Figure 6). As Reference [45] stated: *"an iteration method for correcting base value was supplemented to improve accuracy"*. The linearization error depends on the proximity of the base value to the actual operating point. The iteration corrects the base value toward the actual solution, achieving super-linear convergence with errors typically below 0.3 %.

The convergence threshold ε determines when the iterative process terminates - it defines the acceptable difference between the computed solution and the reference base value. This is conceptually analogous to the tolerance setting in Newton-Raphson power flow methods: a smaller ε yields higher accuracy but requires more iterations. The choice of ε represents a trade-off between computational cost and solution accuracy.

The step size $\gamma \in (0,1]$ controls the update magnitude in each iteration:

$$X_{k+1} = (1-\gamma)X_k + \gamma \bar{X}_k \tag{40}$$

where $X_k$ is the current base value and $\bar{X}_k$ is the newly computed value. This formulation follows the standard damped iteration or successive over-relaxation principle, where $\gamma = 1$ corresponds to full replacement and $\gamma < 1$ provides damping to prevent oscillation. The theoretical requirement for convergence is that the update maintains stability while progressively reducing the error - a principle widely used in iterative methods for nonlinear systems.

To provide quantitative guidance for parameter selection, we conducted a systematic sensitivity analysis testing different combinations of ε and γ values. Ten step size values were tested: $\gamma = \{0.1, 0.2, 0.3, 0.4, 0.5, 0.6, 0.7, 0.8, 0.9, 1.0\}$, and six convergence thresholds were tested: $\varepsilon = \{0.01, 0.02, 0.05, 0.1, 0.15, 0.2\}$ m/s. The results are summarized in Tables 1 and 2: where $\gamma = 0.6$ provides the optimal balance - converging within 8 iterations with stable monotonic decrease and minimal final error. $\gamma \leqslant 0.3$ leads to excessively slow convergence (>20 iterations), while $\gamma \geqslant 0.8$ introduces oscillatory behavior due to over-correction, occasionally causing divergence.

The results are insensitive to $\varepsilon$ variations as long as $\varepsilon \leqslant 0.1$. Reducing $\varepsilon$ from 0.1 to 0.01 improves accuracy by less than 0.02 % but increases iteration count by 30-40 %. Therefore, $\varepsilon = 0.1$ is selected as the practical engineering threshold.

**Table 1** Final relative error (%)

| γ \ ε | 0.01 | 0.02 | 0.05 | **0.1** | 0.15 | 0.2 |
|---|---|---|---|---|---|---|
| 0.2 | 0.05 | 0.06 | 0.07 | 0.08 | 0.10 | 0.12 |
| 0.3 | 0.04 | 0.05 | 0.06 | 0.07 | 0.09 | 0.11 |
| 0.4 | 0.04 | 0.04 | 0.05 | 0.06 | 0.08 | 0.10 |
| 0.5 | 0.03 | 0.04 | 0.04 | 0.05 | 0.07 | 0.09 |
| **0.6** | 0.03 | 0.03 | 0.04 | 0.05 | 0.07 | 0.09 |
| 0.7 | 0.04 | 0.04 | 0.05 | 0.06 | 0.08 | 0.11 |
| 0.8 | 0.05 | 0.05 | 0.06 | 0.07 | 0.10 | 0.14 |
| 0.9 | 0.07 | 0.08 | 0.08 | 0.10 | 0.13 | 0.18 |
| 1.0 | 0.10 | 0.11 | 0.11 | 0.12 | 0.16 | 0.22 |

**Table 2** Convergence speed and accuracy under different γ values (ε = 0.1)

| γ | Iterations to converge | Final relative error |
|---|---|---|
| 0.1 | 35 | 0.09 % |
| 0.2 | 22 | 0.08 % |
| 0.3 | 16 | 0.07 % |
| 0.4 | 13 | 0.06 % |
| 0.5 | 10 | 0.05 % |
| **0.6** | 8 | 0.05 % |
| 0.7 | 8 | 0.06 % |
| 0.8 | 9 | 0.07 % |
| 0.9 | 8 | 0.10 % |
| 1.0 | 7 (occasional divergence) | 0.12 % |

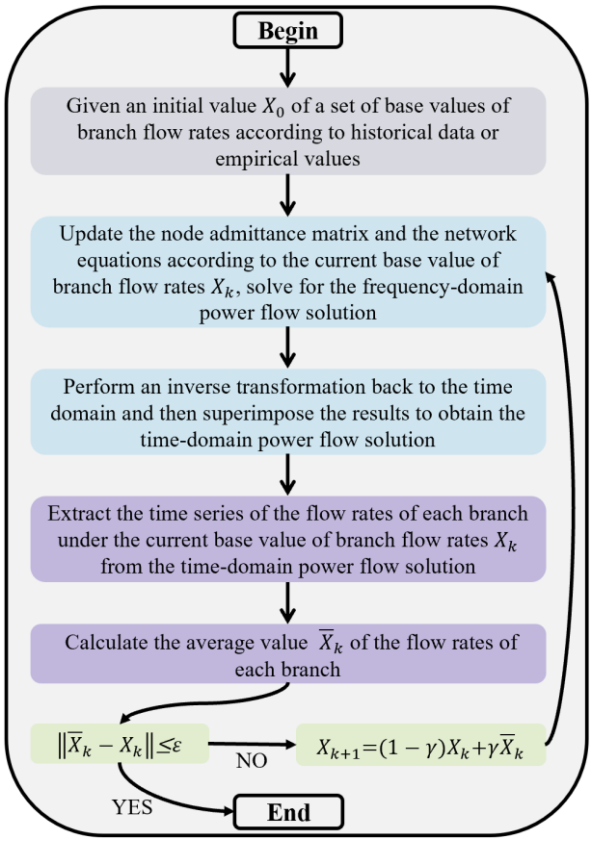



**Fig. 6** Base value correction method

## 2.2 Gas-electric network joint economic low-carbon dispatch model

### 2.2.1 Objective function

The gas-electric network joint economic dispatch model established in this paper solves the Pareto front of the economic-carbon emission bi-objective optimization using the $\varepsilon$-constraint method. The $\varepsilon$-constraint method retains one objective as the objective function and converts the remaining objectives into constraints. The objective function is to minimize the economic cost, with the constraint that carbon emissions $\leq \varepsilon$. By traversing different $\varepsilon$ values, a series of optimal solutions are obtained, forming the Pareto front. The single optimization formulation of the $\varepsilon$-constraint method is as follows:

$$\begin{aligned} &\min Z = \sum_{g=1}^{N_G}\sum_{t=1}^{T}\left[\sum_{s=1}^{S} c_{g,s}\cdot P_{g,t,s}^{seg}\cdot\Delta t + C_g^{SS}\cdot v_{g,t}\right] \\ &s.t.\sum_{g=1}^{N_G}\sum_{t=1}^{T}\left(\varepsilon_g\cdot P_{g,t}\cdot\Delta t\right)\leq\varepsilon \end{aligned} \tag{41}$$

where $T$ represents the total number of optimization time intervals (96 intervals of 15 minutes each). $S$ represents the number of piecewise linearization segments (20 segments), and $s$ is the segment index. $N_G$ represents the total number of generator units (6 units). $v_{g,t} \in [0,1]$ indicates the start-up status of unit $g$ at time interval $t$, being 1 when starting up. $c_{g,s}$ represents the incremental cost slope of unit $g$ at segment $s$, in USD/kWh. $P_{g,t,s}^{\text{seg}}$ represents the output power of unit $g$ at time interval $t$ in segment $s$, in kW. $C_g^{\text{SS}}$ represents the single start-up/shut-down cost of unit $g$, in USD per start. $\varepsilon_g$ represents the carbon

emission intensity of unit $g$, in kg/kWh. $P_{g,t}$ is the total output of unit $g$ at time interval $t$, in kW. $\varepsilon$ is the upper limit of carbon emissions, in kg. $\Delta t$ is the time interval, $\Delta t$=15/60(hours).

2.2.2 Constraint conditions

1. Power system constraints

(1) Node power balance

$$\sum_{g\in\mathcal{G}_b} P_{g,t} - P_{load,n,t} = \sum_{b\in\mathcal{B}_n} P_{f,b,t}\cdot\sigma_{n,b}\,,\forall n,t \tag{42}$$

where $G_b$ is the set of units connected to node $n$; $\mathcal{B}_n$ is the set of branches connected to node $n$; $P_{load,n,t}$ is the load demand at node $n$ during time interval $t$; $P_{f,b,t}$ is the power flow of branch $b$ during time interval $t$ (kW). $\sigma_{n,b}$ is the node-branch incidence factor:

$$\sigma_{n,b} = \begin{cases} +1, & \text{if bus } n \text{ is the from-bus of branch } b \\ -1, & \text{if bus } n \text{ is the to-bus of branch } b \\ 0, & \text{otherwise} \end{cases}$$

(2) DC power flow constraints

The shipboard power system considered in this study operates at medium voltage (660~720 V) with relatively short cable lengths. The per-unit resistance and reactance of the cables are 0.0057 p.u. and 0.004 p.u., respectively, yielding an R/X ratio of approximately 1.43. According to established power system literature, DC power flow provides acceptable accuracy when the R/X ratio is less than 3.0, as the coupling between active power and voltage angle remains dominant 43.

$$\begin{aligned} &\frac{P_{f,b,t}}{S_{base}} = B_b\cdot\left(\theta_{from,b,t}-\theta_{to,b,t}\right),\forall b,t \\ &-P_{f,b}^{max} \le P_{f,b,t} \le P_{f,b}^{max},\forall b,t \end{aligned} \tag{43}$$

where $S_{base}$ is the power base (MVA); $B_b$ is the susceptance of branch $b$ (p.u.); $\theta_{from,b,t}$ is the phase angle at the from-bus of branch $b$ during time interval $t$; $\theta_{to,b,t}$ is the phase angle at the to-bus of branch $b$ during time interval $t$; $P_{f,b}^{max}$ is the upper limit of power flow on branch $b$ (kW).

The susceptance matrix describes the susceptance relationships among nodes in the power network. Its mathematical expression is:

$$B_b = \begin{cases} -\frac{1}{X_{b,n}} \\ \sum_{k\neq b}\frac{1}{X_{b,k}} \end{cases} \tag{44}$$

where $B_{b,n}$ is the susceptance between nodes $b$ and $n$; $X_{b,n}$ is the reactance of line $b-n$. Off-diagonal elements are mutual susceptances: $B_{b,n}=B_{n,b}=-1/X_{b,n}$; diagonal elements are self-susceptances: $B_{b,b}=\sum_{k\neq b}1/X_{b,k}$.

Voltage phase angle constraints:

$$-\frac{\pi}{4} \le \theta_{b,t} \leqslant \frac{\pi}{4} \tag{45}$$

(3) Output limits

$$\sum_{g=1}^{N_G} P_{g,min}\cdot u_{g,t} \le P_{load}(t) \le \sum_{g=1}^{N_G} P_{g,max}\cdot u_{g,t},\forall t \tag{46}$$

where $u_{g,t} \in [0,1]$ is the on/off status of unit $g$ during time interval $t$ (1 when running); $P_{g,min}$, $P_{g,max}$ are the minimum and maximum outputs of unit $g$ (kW).

(4) Ramp rate constraints

$$-\Delta P_g^{max} \le P_{g,t} - P_{g,t-1} \le \Delta P_g^{max}, \forall g, t \ge 1 \tag{47}$$

$$\Delta P_g^{max} = RampRate_g \cdot 60 \cdot \Delta t \tag{48}$$

where $\Delta P_g^{max}$ is the maximum ramp rate of unit $g$ (kW); $RampRate_g$ is the ramp speed (kW/min).

(5) Unit output and start-down status correlation constraint

$$P_{g,min} \cdot u_{g,t} \le P_{g,t} \le P_{g,max} \cdot u_{g,t}, \forall g, t \tag{49}$$

where $P_{g,t}$ represents the output of unit $g$ at time $t$ (kW).

(6) Start-down status constraints

$$\begin{aligned} v_{g,t} &\ge u_{g,t} - u_{g,t-1,}\ \forall g, t \ge 1 \\ v_{g,t} &\ge u_{g,t-1} - u_{g,t}\ \forall g, t \ge 1 \\ w_{g,t} &\ge u_{g,t-1} - u_{g,t}, \forall g, t \ge 1 \\ w_{g,t} &\le u_{g,t-1}, \forall g, t \ge 1 \\ w_{g,t} &\le 1 - u_{g,t}, \forall g, t \ge 1 \end{aligned} \tag{50}$$

where $v_{g,t}$ is the start-up indicator of unit $g$ at time $t$ (1 when starting up); $w_{g,t}$ is the shut-down indicator of unit $g$ at time $t$ (1 when shutting down).

(7) Minimum start-down time constraints

$$\begin{aligned} \textstyle\sum_{k=t-T_{up}+1}^{t} u_{g,k} &\ge T_{up} \cdot v_{g,t}, \forall g, t \ge T_{up} \\ \textstyle\sum_{k=t-T_{down}+1}^{t} \left(1 - u_{g,k}\right) &\ge T_{down} \cdot w_{g,t}, \forall g, t \ge T_{down} \end{aligned} \tag{51}$$

where $T_{up}$ is the minimum start-up time; $T_{down}$ is the minimum shut-down time.

2. Piecewise linearization parameter calculation

(1) Breakpoint calculation

$$P_k = P_{min} + k \cdot \frac{P_{max} - P_{min}}{N}, k = 0,1,2, \dots, N \tag{52}$$

where $P_k$ is the power value at the $k$-th breakpoint; $P_{min}/P_{max}$ are the minimum/maximum output of the unit; $N$ is the number of segments.

(2) Segment width calculation

$$\Delta P_s = P_{s+1} - P_s, s = 1,2, \dots, N \tag{53}$$

where $\Delta P_s$ is the width of segment $s$; $P_s$ is the power value at the $s$-th breakpoint.

(3) Cost function value calculation

$$\begin{aligned} f(P) &= \alpha P^2 + \beta P + \gamma \\ f_k &= \alpha P_k^2 + \beta P_k + \gamma \\ f_{k+1} &= \alpha P_{k+1}^2 + \beta P_{k+1} + \gamma \end{aligned} \tag{54}$$

where $f(P)$ is the generation cost function of the unit; $\alpha$ is the quadratic cost coefficient; $\beta$ is the linear cost coefficient; $\gamma$ is the fixed cost coefficient.

(4) Incremental slope calculation

$$s_k = \frac{f_{k+1} - f_k}{P_{k+1} - P_k} \tag{55}$$

where $s_k$ is the incremental cost slope of segment $k$; $f_{k+1}$is the cost value at breakpoint $P_{k+1}$; $f_k$ is the cost value at breakpoint $P_k$; $P_{k+1}$ is the power value at the $(k+1)$-th breakpoint; $P_k$ is the power value at the $k$-th breakpoint.

3. Natural gas system constraints

(1) Gas consumption calculation of gas-fired units

$$Q_{g,t} = \frac{r_{gas} \cdot P_{g,t}}{3600}, g \in \{GT1, GT2\} \tag{56}$$

where $Q_{g,t}$ is the gas consumption of unit $g$ during time interval $t$ (kg/s); $r_{gas}$ is the gas consumption rate (kg/kWh); $P_{g,t}$ is the output of unit $g$ during time interval $t$ (kW).

(2) Gas network node pressure and flow constraints

$$G_n^{Gmin} \le G_{n,t}^G \le G_n^{Gmax} \tag{57}$$

$$P_n^{Gmin} \le P_{n,t}^G \le P_n^{Gmax} \tag{58}$$

where $G_{n,t}^G$ is the gas flow at node $n$ of the natural gas network during time interval $t$; $G_n^{Gmin}$ and $G_n^{Gmax}$ are the lower and upper limits of gas flow at node $n$; $P_{n,t}^G$ is the gas pressure at node $n$ of the natural gas network during time interval $t$; $P_n^{Gmin}$ and $P_n^{Gmax}$ are the lower and upper limits of gas pressure at node $n$.

4. Carbon emission calculation

(1) Unit carbon emissions

$$E_g = \sum_{t=1}^{T} \varepsilon_g \cdot P_{g,t} \cdot \Delta t, \ \forall g \tag{59}$$

where $E_g$ is the total carbon emission of unit $g$ (kg); $\varepsilon_g$ is the carbon emission intensity of unit $g$ (kg/kWh).

(2) Unit carbon emission cost

$$C_g^{carbon} = E_g \cdot P_{CO_2}, \forall g \tag{60}$$

where $C_g^{carbon}$ is the carbon emission cost of unit $g$ (USD); $P_{CO_2}$ is the carbon emission price (USD/kg).

### 2.2.3 Model solution

The proposed gas-electric joint economic dispatch model loads power and gas network parameters, then uses the $\varepsilon$-constraint method to obtain the economic-carbon Pareto front. First, the purely economic and purely low-carbon optima are found (zero weights for emissions and cost, respectively). Adaptive sampling is performed within the resulting emission interval. For each $\varepsilon$, a gas-electric closed-loop tightening MILP is executed: Gurobi (1800 s, 1 % gap, 4 threads) produces unit schedules; time-frequency domain dynamic gas power flow calculates node pressures. If any gas-consuming node pressure violates limits, the corresponding gas-fired unit's gas consumption upper bound is tightened, total supply bound is updated, and the process repeats. Upon convergence, total cost and emissions for that $\varepsilon$ are recorded. A coarse scan (5 points) plus adaptive refinement yields the complete Pareto front. The normalized distance method selects the compromise point. Optimization results for different scenarios are generated, including unit output comparisons and gas network node flow/pressure time-domain curves, demonstrating the impact of dynamic gas constraints on economy and emissions (Figure 7).

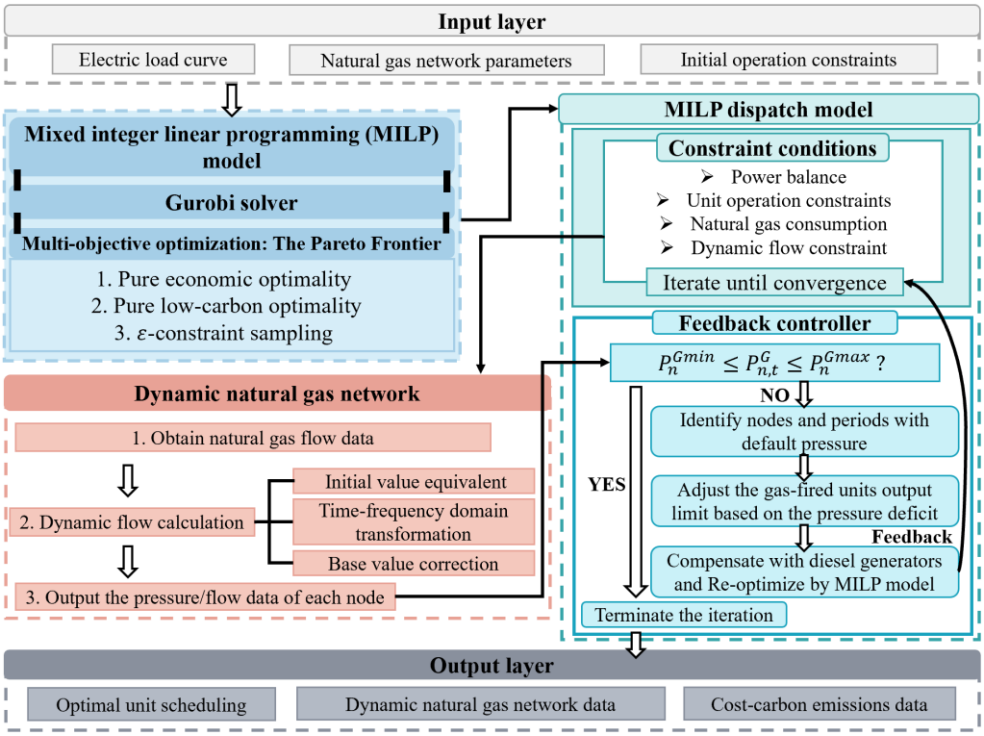



**Fig. 7** Model solution

1. Pressure Violation Detection

At each iteration $k$, after solving the frequency-domain gas network equations, a violation is detected if:

$$P_{n,t}^{(k)} > P_n^{\max} + \delta \tag{61}$$

where $P_{n,t}^{(k)}$ is the computed pressure at node $n$ during period $t$ at iteration $k$ (MPa), $P_n^{\max}$ is the upper pressure limit at node $n$ (MPa), and $\delta = 0.001$ MPa is the allowable pressure tolerance, introduced to prevent over-tightening due to negligible numerical errors.

The violation magnitude is defined as:

$$\Delta P_{n,t}^{(k)} = P_{n,t}^{(k)} - P_n^{\max} \tag{62}$$

where $\Delta P_{n,t}^{(k)}$ is the pressure violation magnitude at iteration $k$ (MPa).

2. Tightening of Gas Consumption Upper Bounds

When a pressure violation is detected at node $n$, the gas consumption upper bounds for all gas-fired units $g$ connected to node $n$ are tightened according to:

$$Q_{g,t}^{\max,(k+1)} = Q_{g,t}^{\max,(k)} - \beta \cdot \frac{\Delta P_{n,t}^{(k)}}{P_n^{\max} - P_n^{\min}} \cdot Q_{g,t}^{\max,(k)} \tag{63}$$

where $Q_{g,t}^{\max,(k)}$ is the current upper bound on gas consumption of unit $g$ at time $t$ at iteration $k$ (kg/s), $P_n^{\min}$ is the lower pressure limit at node $n$ (MPa), and $\beta$ is the tightening coefficient (dimensionless).

The normalized equivalent form is:

$$Q_{g,t}^{\max,(k+1)} = Q_{g,t}^{\max,(k)} \cdot \left(1 - \beta \cdot \frac{\Delta P_{n,t}^{(k)}}{P_n^{\max} - P_n^{\min}}\right) \tag{64}$$

3. Upper and Lower Bound Protection

To prevent over-tightening that could lead to infeasibility, the following safeguards are applied:

$$Q_{g,t}^{\max,(k+1)} \geq Q_{g,t}^{\min} \tag{65}$$

$$Q_{g,t}^{\max,(k+1)} \leq Q_{g,t}^{\max,(0)} \tag{66}$$

where $Q_{g,t}^{\min} = H_g \cdot P_{g,\min}$ is the minimum gas consumption corresponding to the minimum stable output of the gas-fired unit (kg/s), $H_g$ is the hydrogen consumption rate of unit $g$ (kg/kWh), $P_{g,\min}$ is the minimum output power of unit $g$ (kW); and $Q_{g,t}^{\max,(0)}$ is the initial upper bound, i.e., the physical pipeline capacity (kg/s).

4. Adaptive Tightening Coefficient

The tightening coefficient $\beta$ is adaptively adjusted to balance convergence speed and stability:

$$\beta = \begin{cases} 0.3, & k = 1 \text{ (first violation)} \\ 0.5, & 2 \leq k \leq 5 \text{ (persistent violation)} \\ 0.7, & k > 5 \text{ (stubborn violation)} \end{cases} \tag{67}$$

where $k$ is the current iteration number.

This adaptive strategy ensures: Conservative tightening initially ($\beta = 0.3$) to avoid over-correction; Moderate tightening for persistent violations ($\beta = 0.5$) to accelerate convergence; Aggressive tightening for stubborn cases ($\beta = 0.7$) to force constraint satisfaction.

5. Multiple Violation Handling

If multiple nodes experience pressure violations simultaneously, the most restrictive tightening is applied:

$$Q_{g,t}^{\max,(k+1)} = \min_{n \in \mathcal{N}_{\text{viol}}} \left\{ Q_{g,t}^{\max,(k)} \cdot \left( 1 - \beta \cdot \frac{\Delta P_{n,t}^{(k)}}{P_n^{\max} - P_n^{\min}} \right) \right\} \tag{68}$$

where $\mathcal{N}_{\text{viol}}$ is the set of nodes with pressure violations.

6. Convergence Criteria

The closed-loop iterative tightening terminates when ALL of the following conditions are satisfied:

Condition 1 – Pressure constraints satisfied:

$$P_n^{\min} - \delta \leq P_{n,t}^{(k)} \leq P_n^{\max} + \delta, \ \forall n, \forall t \tag{69}$$

Condition 2 – Gas consumption change negligible:

$$\max_{g,t} \left| \frac{Q_{g,t}^{(k)} - Q_{g,t}^{(k-1)}}{Q_{g,t}^{(k-1)}} \right| \leq \eta \tag{70}$$

where $\eta = 0.5\%$ is the allowable relative change threshold, and $Q_{g,t}^{(k)}$ is the gas consumption of unit $g$ at time $t$ at iteration $k$ (kg/s).

Condition 3 – Maximum iterations not exceeded:

$$k \leq K_{\max} = 20 \tag{71}$$

where $K_{\max}$ is the maximum number of iterations.

If the maximum iteration count is reached without satisfying Conditions 1 and 2, the "safe relaxation" mechanism is activated (described in Section 7 below).

## 7. Convergence Analysis and Feasibility Analysis

The convergence of the iterative framework can be analyzed from the perspective of contraction mapping. Define the gas consumption upper bound vector at the $k$-th iteration as $Q^{(k)} = \left[Q_{g,t}^{\max,(k)}\right]$, and the tightening mapping $\mathcal{T}$ as:

$$Q^{(k+1)} = \mathcal{T}\left(Q^{(k)}\right) \tag{72}$$

The tightening mapping $\mathcal{T}$ is composed of three sequential operations. First, the tightening operator directly reduces the gas consumption upper bound based on the pressure violation magnitude: $Q^{\max,(k+1)} = Q^{\max,(k)} - \beta \cdot (\Delta P/\Delta P_{\max}) \cdot Q^{\max,(k)}$. Second, the projection operator enforces upper and lower bound protection to prevent over-tightening that could lead to infeasibility: $Q^{\max,(k+1)} = \max\left\{Q^{\min}, \min\left\{Q^{\max,(k+1)}, Q^{\max,(0)}\right\}\right\}$. Third, the constraint propagation operator maps the tightened gas consumption back to nodal pressure through the gas network dynamic power flow equations, completing one full iteration of the tightening mechanism.

The tightening operator directly reduces the gas consumption upper bound ($\beta > 0$, $\Delta P > 0$), so $Q_{g,t}^{\max,(k+1)} \le Q_{g,t}^{\max,(k)}$, meaning the feasible region monotonically shrinks. The monotonic decrease in the gas consumption upper bound ensures that the pressure violation magnitude $\Delta P_{n,t}^{(k)}$ monotonically decreases with increasing iterations until the pressure constraints are satisfied.

When $k \to \infty$ and $\Delta P_{n,t}^{(k)} \to 0$, the tightening update $\beta \cdot (\Delta P/\Delta P_{\max}) \cdot Q^{\max} \to 0$, i.e., $\| Q^{(k+1)} - Q^{(k)} \| \to 0$. Since all components are non-negative and have a lower bound $Q^{\min}$, the sequence $\left\{Q^{(k)}\right\}$ is monotonically decreasing and bounded below; by the Monotone Convergence Theorem, it must converge.

Let the maximum pressure violation at the $k$-th iteration be $\Delta P_{\max}^{(k)} = \max_{n,t}\max\left(0, P_{n,t}^{(k)} - P_n^{\max}\right)$. From the tightening formula, the reduction in the gas consumption upper bound is proportional to $\Delta P_{\max}^{(k)}$. Assuming the gas network pressure has Lipschitz continuity with respect to gas consumption changes (Lipschitz constant $L_P$), i.e., $\| \Delta P \| \le L_P \| \Delta Q \|$, the pressure residual satisfies:

$$\Delta P_{\max}^{(k+1)} \le L_P \cdot \beta \cdot \frac{\Delta P_{\max}^{(k)}}{\Delta P_{\max}} \cdot \Delta P_{\max}^{(k)} \tag{73}$$

Defining the contraction factor $\rho = L_P \cdot \beta \cdot \left(\Delta P_{\max}^{(k)}/\Delta P_{\max}\right)$, when $\rho < 1$, the iteration exhibits linear convergence:

$$\Delta P_{\max}^{(k)} \le \rho^k \cdot \Delta P_{\max}^{(0)} \tag{74}$$

Since $\beta = 0.3, 0.5, 0.7$ and $\Delta P_{\max}^{(k)}/\Delta P_{\max} < 1$, in practice $\rho < 0.7$ is satisfied, ensuring linear convergence of the iteration. This convergence rate reduces the pressure residual to an acceptable level within 8–10 iterations, consistent with numerical experiments (8 iterations).

During the gas-electric closed-loop iteration process, the gas consumption upper bound of gas-fired units is continuously tightened due to pressure violations. To ensure that the optimization problem remains feasible (i.e., the feasible region is non-empty), the diesel generators must have sufficient adjustable capacity to compensate for the power deficit caused by the reduction in gas-fired unit output.

Let the maximum available output of gas-fired units at a given period due to gas network pressure violations be $P_{\text{gas}}^{\max}(t)$. The system power deficit is:

$$\Delta P_t = P_{\text{load}}(t) - P_{\text{gas}}^{\max}(t) \tag{75}$$

The total adjustable capacity of diesel units is:

$$C_{\text{diesel}}^{\text{total}} = \sum_{g \in \mathcal{G}_{\text{diesel}}} \left( P_{g,\max} - P_{g,\min} \right) \tag{76}$$

To guarantee a non-empty feasible region, the system must satisfy at any period:

$$\sum_{g \in \mathcal{G}_{\text{diesel}}} \left( P_{g,\max} - P_{g,\min} \right) \geq \Delta P_t + R \cdot P_{\text{load}}(t), \ \forall t \tag{77}$$

where $R$ is the reserve capacity coefficient (taken as $R = 10\ \%$ in this study). When this condition is satisfied, even if gas-fired unit output drops to its minimum, the diesel units still have sufficient capacity to meet the load demand, ensuring the feasibility of the optimization problem.

In the hybrid ship system studied in this work, the total diesel unit capacity is $4 \times 16.8 = 67.2$ MW, the total gas-fired unit capacity is $2 \times 25 = 50$ MW, and the peak load is 120 MW. In the most extreme case (all gas-fired units offline), diesel units can still provide 67.2 MW; the deficit is covered by load regulation and reserve capacity. In actual dispatch, gas-fired unit output cannot drop to zero (due to minimum stable output constraints), and load peaks are transient, so this sufficient condition is satisfied in all test cases of this study.

8. Safety Relaxation Mechanism

In cases where strict constraint satisfaction is infeasible (e.g., extreme load conditions exceeding pipeline capacity), the following safety relaxation rule is applied:

Relaxation trigger:

$$k = K_{\max} = 20 \text{ and } \exists (n,t) \text{ such that } P_{n,t}^{(k)} > P_n^{\max} + \delta \tag{78}$$

Relaxation rule:

$$Q_{g,t}^{\max,\text{relax}} = Q_{g,t}^{\max,(0)} \cdot \min\left(1, +\alpha_{\text{relax}} \frac{P_{n,t}^{(k)}}{P_n^{\max}}\right)^{-1} \tag{79}$$

where $\alpha_{\text{relax}} = 5\%$ is the maximum allowable over-limit gas consumption, and the relaxation is permitted for a maximum duration of 10 minutes (1 time interval).

Relaxation termination: The relaxation is automatically revoked in the next iteration once the pressure violation is resolved.

## 3. Proposed method and numerical results

### 3.1 Basic parameter example

This chapter presents a 4-node (N1-N4), 3-branch (B1-B3) natural gas network (Figure 8; arrows indicate flow direction). Branch B1 has a booster ($E_b$= 2 MPa); pipeline parameters are in Table 3. Node 1 is a constant-pressure source (0.5 MPa); pressures and flow velocities at other nodes are indirectly regulated by gas-consuming nodes.

Nodes 2, 3, 4 are negative gas flow sources (reference consumption 1.48 kg/s), varying stepwise by $\pm$ 20 % at 1-hour intervals (Figure 9; absolute values are shown for clarity).

The simulation runs for 24 hours (96 intervals of 15 minutes). An additional 12 hours of historical boundary conditions are used to establish initial conditions, but only the effective 24-hour period is shown in figures (same for other similar cases).

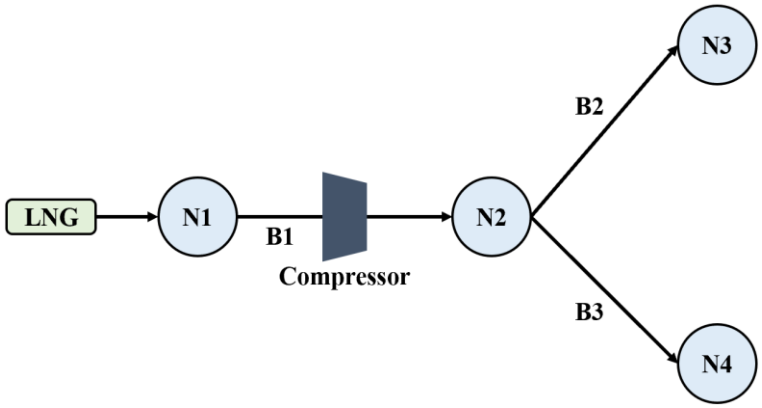



**Fig. 8** Natural gas network structure

**Table 3** Pipeline parameters

| Pipeline | Length (km) | Inner diameter (m) | Roughness | Flow velocity base value (m/s) | Compressor (MPa) | Pipeline inclination angle (°) |
|---|---|---|---|---|---|---|
| B1 | 0.07 | 0.207 | 0.02 | 15.0 | 2 | 0 |
| B2 | 0.035 | 0.0932 | 0.015 | 15.0 | 0 | 0 |
| B3 | 0.03 | 0.0932 | 0.015 | 15.0 | 0 | 0 |

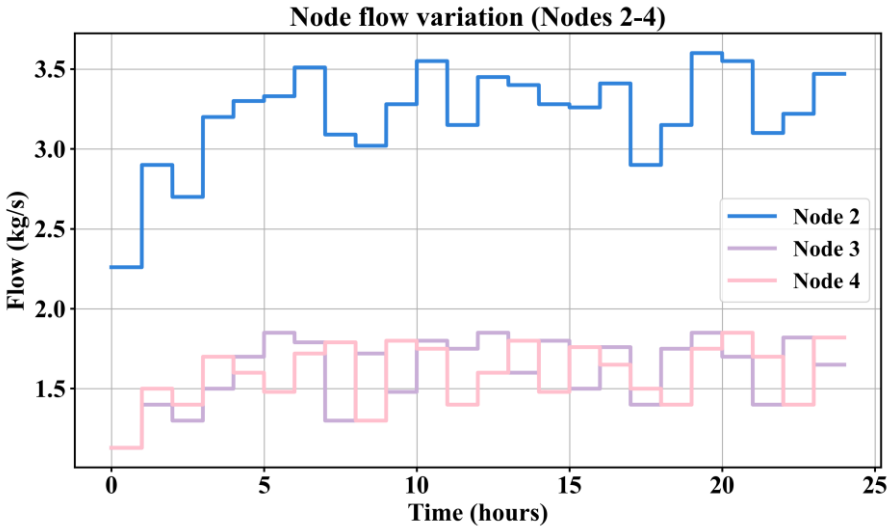



**Fig. 9** Flow variation curves of each gas-consuming node

Fast Fourier transform (FFT) is applied to the gas consumption curves of nodes 2, 3, and 4 to extract sinusoidal alternating gas flow sources at different frequencies. Using node 3 as an example, its frequency spectrum (Figure 10) shows rapid amplitude decay with increasing frequency; by the $100^{th}$ component, the amplitude falls below 5 % of the peak. Thus, truncating to the first 100 components keeps computational error small. Node 1 has constant pressure and does not require FFT.

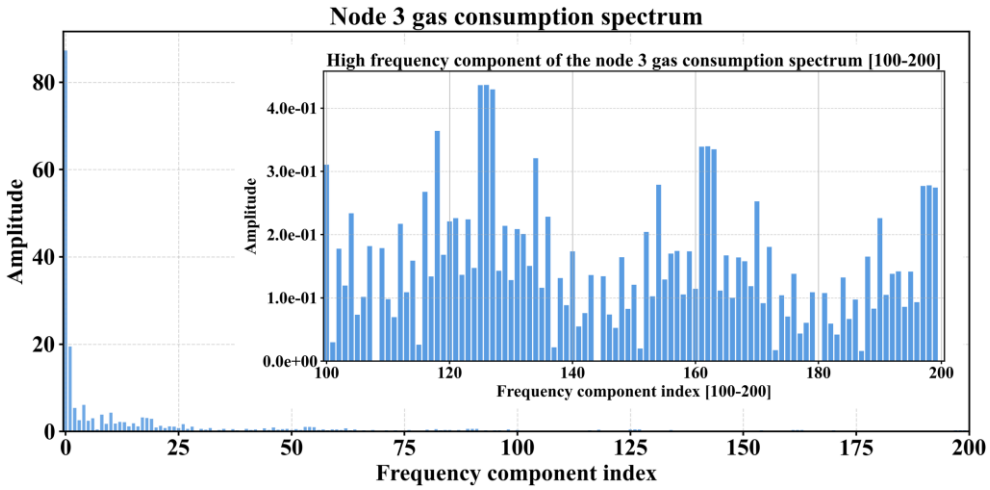



**Fig. 10** Frequency spectrum of gas consumption at node N3

## 3.2 Feasibility verification of the proposed gas network model

### 3.2.1 Grid convergence analysis

To verify the reliability of FDM and FEM as benchmarks, we employ the standard methods from the Verification & Validation (V&V) community - Grid Convergence Analysis and Richardson extrapolation - to quantitatively assess the discretization errors of the benchmark solutions.

Grid convergence analysis verifies solution reliability by solving the same problem on three successively refined grids. We performed a three-grid convergence analysis for FDM (coarse: time step 0.15 s, space step 100 m; medium: time step 0.05 s, space step 50 m; fine: time step 0.025 s, space step 25 m s). Using the pressure at Node 2 as the monitored quantity, the observed order of convergence p≈1.58 and the Grid Convergence Index $GCI_{21}$≈2.54×10⁻⁵ (approximately 0.0025 %) were obtained. The ratio $GCI_{32}/(r^p \cdot GCI_{21})$≈1.00 falls within 0.9-1.1, confirming that the solution is in the asymptotic convergence range and the discretization error is well controlled.

To further confirm the reliability of the benchmarks, we performed cross-validation between FDM and FEM on the same physical problem. The two methods are fundamentally different in their mathematical formulations (finite difference vs. finite element); their mutual consistency at the $10^{-4}$ order of magnitude provides strong evidence for their reliability. The results show that the two benchmarks differ by less than $1.2\times10^{-4}$ MPa in nodal pressure and less than $1.4\times10^{-4}$ kg/s in branch flow, confirming their mutual consistency at the $10^{-4}$ order of magnitude.

The above error levels (GCI≈0.0025 %) are far below the typical engineering accuracy requirements for shipboard gas network dispatch problems (on the order of $10^{-2}$ MPa, approximately 1 %). Therefore, the discretization error of FDM has a negligible impact on the optimal dispatch results of this study, and both FDM and FEM are reliable as benchmarks.

### 3.2.2 Comparison of dynamic model methods

To verify the proposed natural gas network model, the initial flow velocity reference for each branch is set to 15 m/s, the correction step size to 0.6, and the convergence threshold to 0.1. For comparison, the finite difference method (time step 0.15 s, space step 50 m) is used.

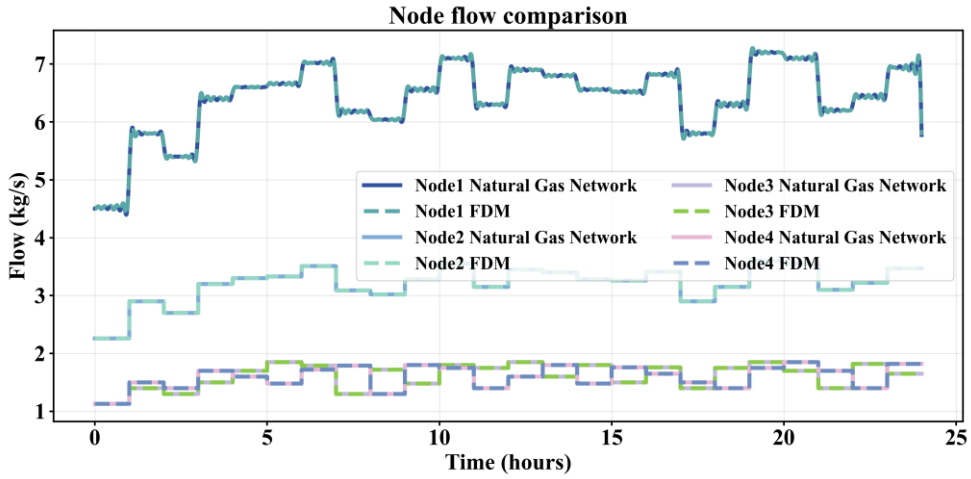



**Fig. 11** Comparison of node flows

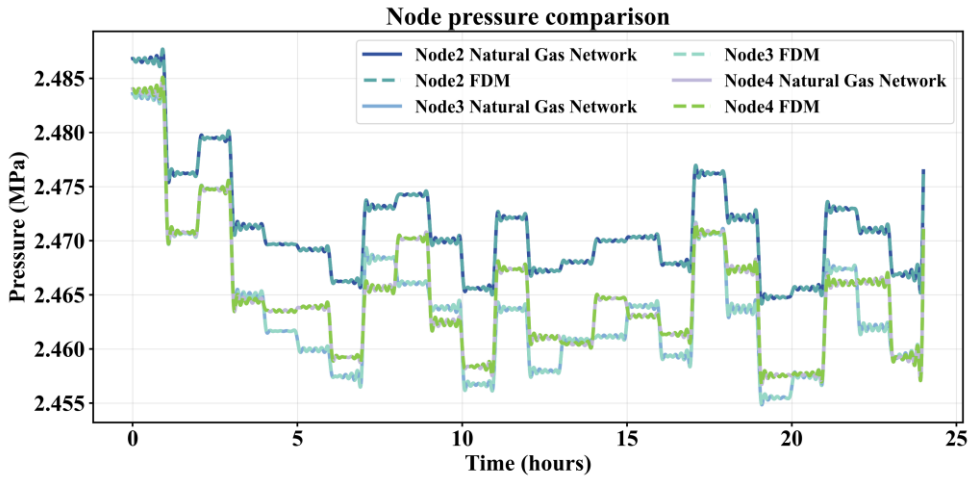



**Fig. 12** Comparison of node pressures

Figures 11 and 12 show high consistency between the proposed natural gas network model and the finite difference method (FDM). Using FDM as the benchmark, the mean absolute errors are $1.29\times10^{-4}$ kg/s (node flow) and $1.24\times10^{-4}$ MPa (node pressure). Computationally, FDM takes 9.89 s, while the proposed model takes only 2.14 s (8 iterations).

For comparison, the finite element method with time and space steps of 0.015 seconds and 20 meters, respectively, is used for calculation.

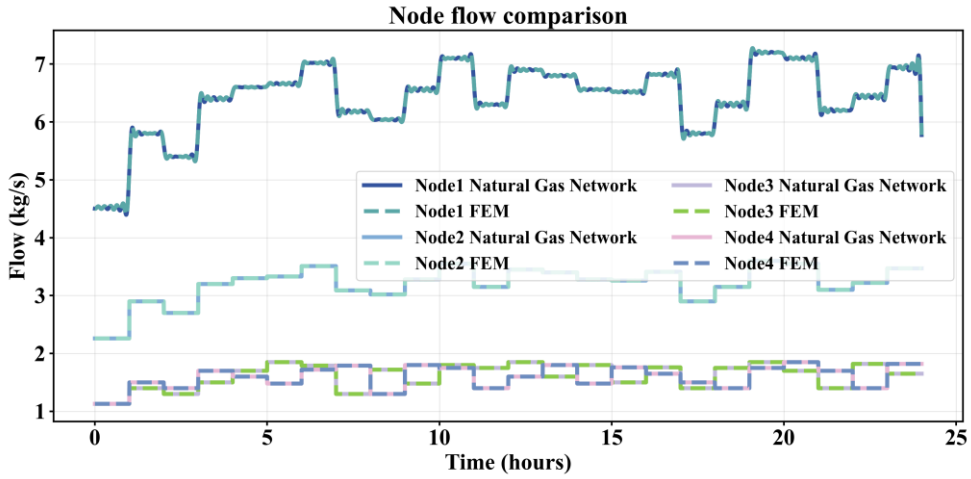



**Fig. 13** Comparison of node flows

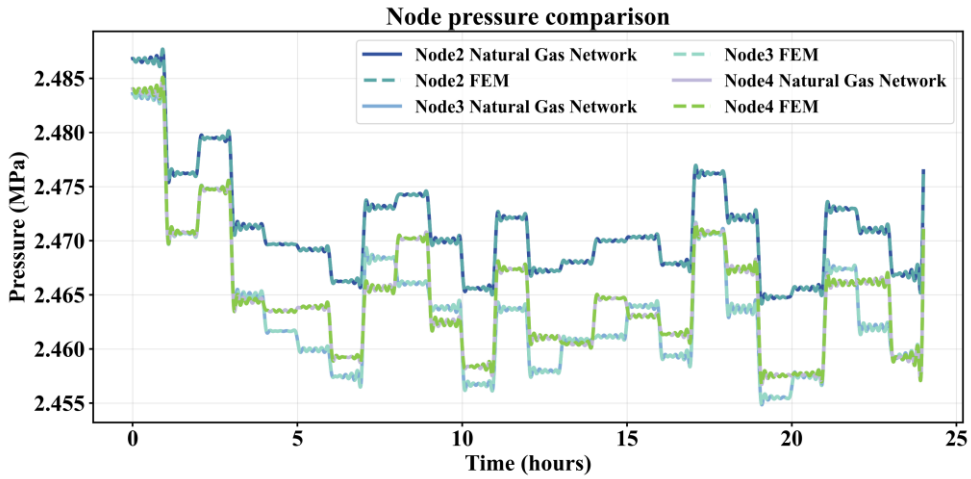



**Fig. 14** Comparison of node pressures

Figures 13 and 14 show high consistency between the proposed natural gas network model and the finite element method (FEM). Using FEM as the benchmark, the mean absolute errors are $1.92\times10^{-4}$ kg/s (node flow) and $1.85\times10^{-4}$ MPa (node pressure). Computationally, FEM takes 7.9 s, while the proposed model takes only 2.14 s (8 iterations).

The method's advantages come from two innovations: (1) time-frequency transformation reduces PDEs to algebraic equations, lowering complexity; (2) branch flow velocity basic value correction method enhances stability while preserving linearization accuracy. This achieves an order-of-magnitude speedup with engineering precision.

Although the 4-node natural gas network validates the principle of the method, we recognize that actual shipboard natural gas networks involve more complex topologies. To further evaluate its scalability, on a 7-node gas network (Figure 15) with longer pipelines and dynamic loads, the method achieves speedups of 5.3× (23.42 s vs. 4.42 s) over finite difference method and 3.5× (15.47 s vs. 4.42 s) over finite element method. Larger networks need further validation, but results show potential for shipboard systems. Future work will use real ship pipeline data for benchmarking.

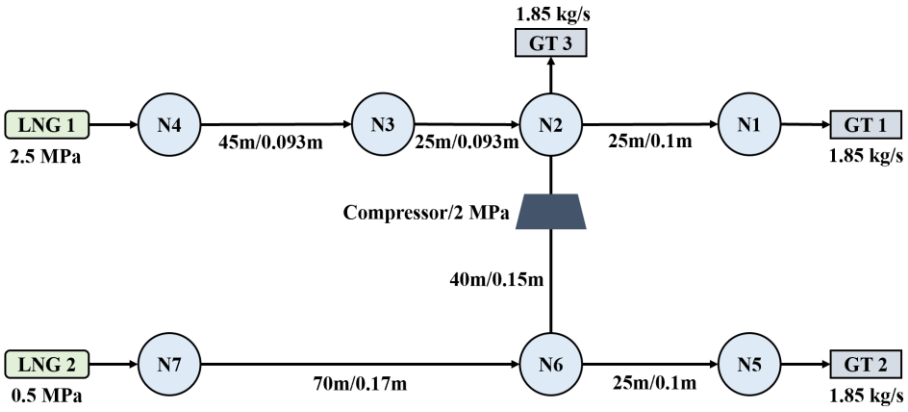



**Fig. 15** 7-node natural gas network

### 3.2.3 Pipeline parameter sensitivity analysis

With other conditions of the natural gas network model unchanged, comparison charts for a 20 % increase in the friction coefficient are obtained using node 2 and branch 2 as examples, with the friction coefficient as the variable.

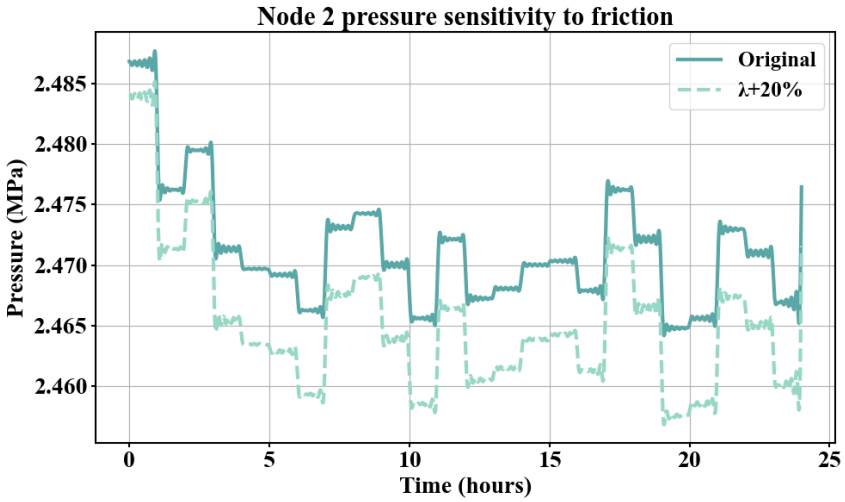



**Fig. 16** Pressure sensitivity of Node 2 to friction coefficient

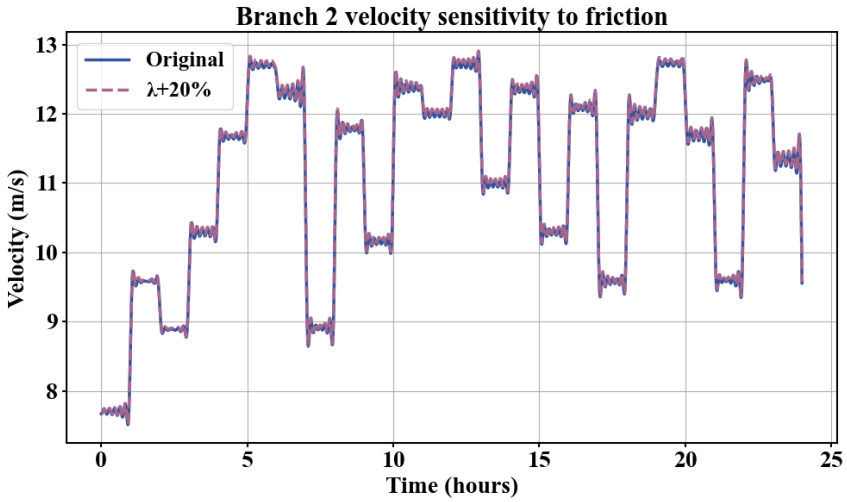



**Fig. 17** Flow velocity sensitivity of Branch 2 to friction coefficient

**Table 4** Sensitivity analysis of friction coefficient

| Friction coefficient ratio | Average pressure (MPa) | Pressure change (%) | Average flow velocity (m/s) | Flow velocity change (%) |
|---|---|---|---|---|
| 0.8 | 2.4770 | 0.24 | 11.06 | -0.24 |
| 0.9 | 2.4741 | 0.12 | 11.07 | -0.12 |
| 1.0 | 2.4711 | 0.00 | 11.09 | 0.00 |
| 1.1 | 2.4682 | -0.12 | 11.10 | 0.12 |
| 1.2 | 2.4652 | -0.24 | 11.12 | 0.24 |

As shown in Figures 16, 17, and Table 4, the friction coefficient has an extremely weak effect on system parameters: a ±20 % change causes only ±0.24 % fluctuations in node-2 pressure and branch-2 flow velocity, with symmetric magnitudes. This low sensitivity is because the shipboard gas network is short-distance; frictional pressure drops in branch 2 (diameter 0.0932 m, length 35 m) is on the order of kPa, far smaller than the MPa-level compressor pressure. Thus, the pressure and flow fields are dominated by gas-source boundary conditions, not internal frictional characteristics.

With other conditions of the natural gas network model unchanged, using pipe diameter as the variable and node 2 and branch 2 as examples, comparison diagrams for a 20 % increase in pipe diameter are obtained.

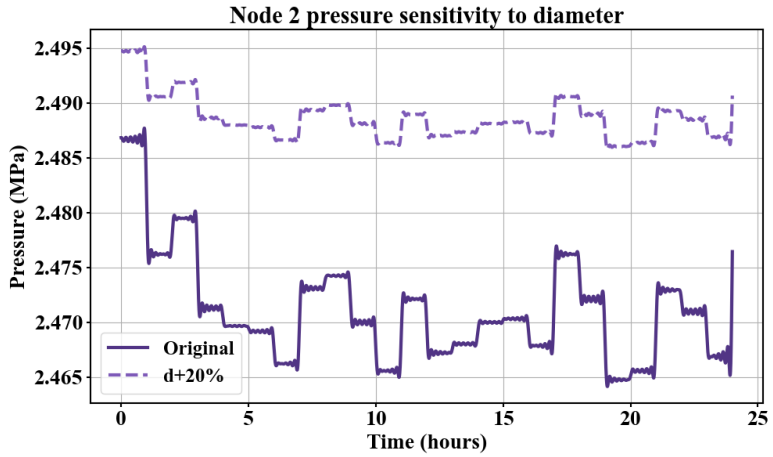



**Fig. 18** Pressure sensitivity of Node 2 to pipe diameter

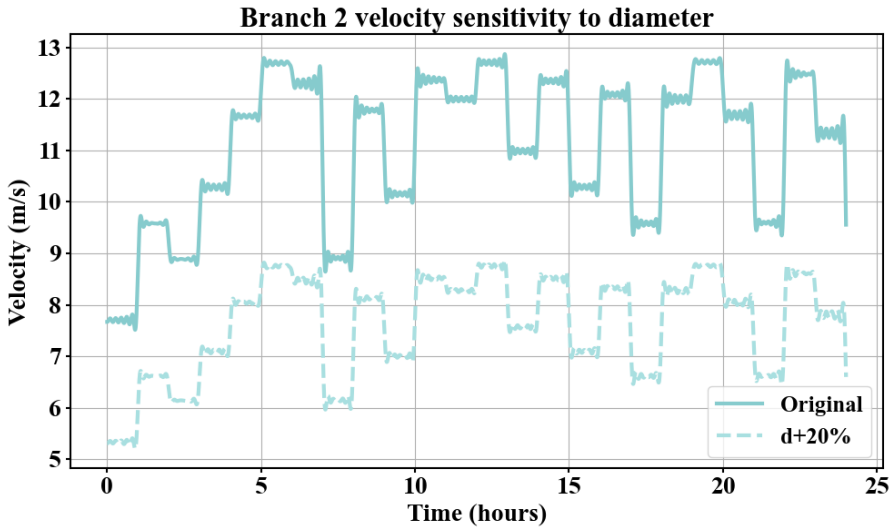



**Fig. 19** Flow velocity sensitivity of Branch 2 to pipe diameter

**Table 5** Sensitivity analysis of pipe diameter

| Pipe diameter ratio | Average pressure (MPa) | Pressure change (%) | Average flow velocity (m/s) | Flow velocity change (%) |
|---|---|---|---|---|
| 0.8 | 2.4076 | -2.57 | 17.79 | 60.45 |
| 0.9 | 2.4503 | -0.84 | 13.81 | 24.52 |
| 1.0 | 2.4711 | 0.00 | 11.09 | 0.00 |
| 1.1 | 2.4822 | 0.45 | 9.12 | -17.73 |
| 1.2 | 2.4886 | 0.71 | 7.65 | -31.05 |

As shown in Figures 18, 19, and Table 5, pipe diameter has an asymmetric influence on hydraulic characteristics. Node 2 pressure is mildly affected: a 20 % diameter reduction decreases pressure by 2.57 %, while a 20 % increase raises it by only 0.71 %, indicating pressure is mainly governed by compressor outlet. In contrast, branch 2 flow velocity changes dramatically: a 20 % diameter reduction increases velocity from 11.09 to 17.79 m/s (+60.45 %); a 20 % increase drops it to 7.65 m/s (-31.05 %). This is due to the inverse square relationship between cross-sectional area and velocity under flow conservation. At baseline 11.09 m/s, a diameter reduction brings velocity close to 18 m/s, near the safe limit for shipboard pipelines.

### 3.2.4 Model assumptions sensitivity analysis

To verify the robustness of the model under different operating conditions and numerical settings, two sensitivity analyses were conducted: (a) linearization error sensitivity under different velocity fluctuation ratios, and (b) historical window length sensitivity.

To quantitatively verify the accuracy of the drag term linearization under different velocity fluctuation levels, we conducted a sensitivity analysis with three scenarios: baseline ($\leq 10$ % deviation), moderate ($\leq 30$ % deviation), and extreme ($\leq 60$ % deviation) fluctuations. Using the FEM fine-grid solution (time step 0.01 s, space step 20 m) as the reference, we compared the proposed model (with base-value correction iteration, 8 iterations) against a fixed linearization model (without iterative correction). The results are summarized in Table 6.

The results demonstrate that: (1) the base-value correction iteration effectively controls the linearization error even under extreme 60 % velocity deviations, maintaining errors below 0.6 %; (2) without iterative correction, the error becomes unacceptably large (up to 20.3 %) under extreme conditions; and (3) under normal ship operating conditions ($\leq 30$ % deviation), the proposed model achieves errors below 0.25 %, well within engineering tolerances. The extreme 60 % deviation case, while rarely encountered in actual ship operations, confirms the robustness of the iterative correction method.

To quantify the impact of the historical window length $T$ on dynamic gas flow calculation accuracy, we conducted a sensitivity analysis with $T = 2,4,6,8,10,12,24$ hours. Using the FEM fine-grid solution as the reference, the pressure errors at $T_0$ and over the full 24-hour horizon were calculated. The results are summarized in Table 7.

The results demonstrate that: (1) the error decreases monotonically with increasing $T$, confirming the convergence of the initial-value equivalent method; (2) when $T \geq 8$ hours, the error falls below 0.12 %, and further increasing $T$ from 12 to 24 hours yields negligible accuracy improvement (< 0.02 %) at the cost of doubled computation time; and (3) $T = 12$ hours provides the optimal balance between accuracy (0.05 % error at $T_0$) and efficiency (2.24 s), making it the recommended value for day-ahead ship dispatch scenarios with 24-hour periodic load profiles.

**Table 6** Sensitivity analysis of pipe diameter

| Scenario | Velocity deviation | Proposed model error (pressure/flow) | Fixed linearization error (pressure/flow) |
|---|---|---|---|
| Baseline | ≤ 10 % | 0.08 % / 0.09 % | 0.15 % / 0.17 % |
| Moderate | ≤ 30 % | 0.21 % / 0.24 % | 2.8 % / 3.1 % |
| Extreme | ≤ 60 % | 0.52 % / 0.58 % | 18.6 % / 20.3 % |

**Table 7** Calculation errors under different historical window lengths T

| Historical window $T$ (h) | Pressure error at $T_0$ | 24-hour average pressure error | Computation time (s) |
|---|---|---|---|
| 2 | 3.42 % | 1.87 % | 1.12 |
| 4 | 1.15 % | 0.62 % | 1.48 |
| 6 | 0.38 % | 0.21 % | 1.82 |

## 4. Gas-electric network joint economic low-carbon dispatch optimization

### 4.1 Basic parameter example

This study focuses on a hybrid cruise ship with two 25 MW gas-fired units, four 16.8 MW diesel units, and two LNG tanks (422.5 $m^3$ each). The four-pod propulsion system (front fixed, rear 360° rotatable) has 21.5 MW AC motors per pod (86 MW total). As shown in Figure 20, pipelines between the gas source/gas-fired units and gas network nodes are neglected. System parameters are in Tables 8-11. The optimization period has 96 15-minute intervals. Carbon price: 0.08 $/kg [47] (based on EU ETS 2024-2025 average price level of approximately €75-85/t $CO_2$); emission factors: gas-fired generators 0.45 kg/kWh [48] (lower bound of CCGT emission factor range 0.45-0.57 kg $CO_2$/kWh), diesel generators 0.68 kg/kWh [49] (mid-range of diesel generator emission factor range 0.6-0.8 kg $CO_2$/kWh); natural gas density: 0.8 kg/$m^3$ (standard conditions: 25°C, 1 atm).

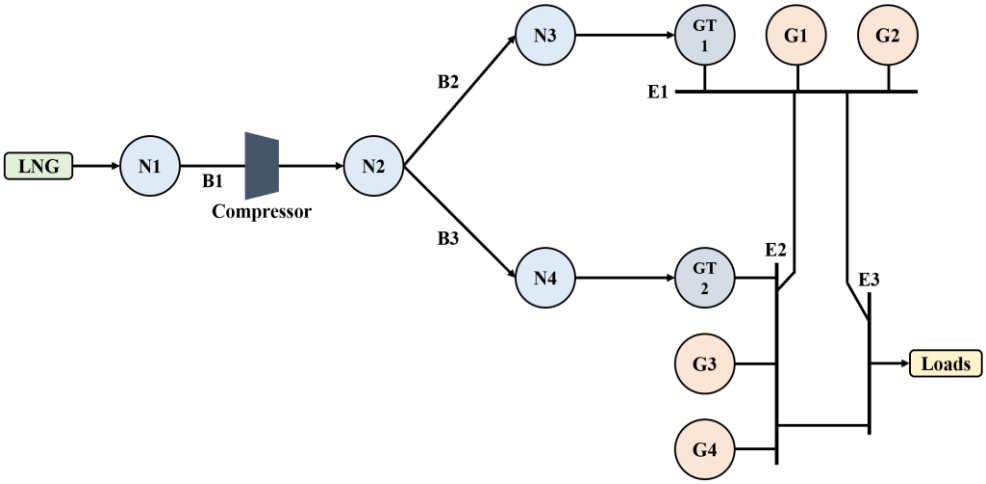



**Fig. 20** Gas-electric joint network structure

**Table 8** Gas network node constraint parameters

| Node | Type | Upper & lower pressure limits (MPa) | Upper & lower of flow (kg/s) |
|---|---|---|---|
| N1 | Constant pressure node | 0.5 | 0~6.59 |
| N2 | Constant flow node | 2.5~2.65 | -3.2~0 |
| N3-N4 | Constant flow node | 2.5~2.65 | -1.65~0 |

**Table 9** Power grid line parameters [50, 51]

| Lines | Resistance (p.u.) | Reactance (p.u.) | Upper limit of power flow (MW) |
|---|---|---|---|
| E1-E2 | 0.0057 | 0.004 | 75 |
| E1-E3 | 0.0057 | 0.004 | 75 |
| E2-E3 | 0.0057 | 0.004 | 75 |

**Table 10** Power system node parameters [43, 51]

| Node | Voltage range (V) | Unit power (MW) | Load power (MW) |
|---|---|---|---|
| E1 | 660~720 | 0~58.6 | - |
| E2 | 660~720 | 0~58.6 | - |
| E3 | 660~720 | - | 0~120 |

**Table 11** Unit parameters [33, 35, 52]

| Unit type | Output range (MW) | Regulation speed (MW/min) | Minimum start-up time (h) | Minimum shut-down time (h) | Unit generation cost (USD/kWh) | | | Start-stop cost (USD) |
|---|---|---|---|---|---|---|---|---|
| | | | | | $\alpha$ | $\beta$ | $\gamma$ | |
| Gas-fired generators | 0~25 | 5 | 1 | 1 | $3\times10^{-6}$ | 0.1 | 50 | 800 |
| Diesel generators | 0~16.8 | 3 | 1 | 1 | $2\times10^{-6}$ | 0.15 | 80 | 1200 |

The parameters in Tables 8-11 are derived from the following sources. The gas network node constraints (Table 8) are based on the IGF Code requirements for LNG fuel gas systems and typical gas turbine inlet pressure specifications. The power grid line parameters (Table 9) are based on CJPJ95 marine cable characteristics (95 mm², 100 m) with per-unit values calculated on a 100 MVA base, referencing [50, 51]. The power system node parameters (Table 10) follow DNV-ST-0373 standards for shipboard medium-voltage power systems, with load profiles derived from typical cruise ship operating conditions [43, 51]. The unit parameters (Table 11) are based on manufacturer specifications for 25 MW gas turbines and 16.8 MW diesel generators, with cost coefficients fitted from typical generator cost curves [33, 35, 52].

## 4.2 Case analysis with and without dynamic gas network constraints

To analyze the impact of dynamic gas network constraints on the optimal dispatch results of the model, the following two cases are set up.

Case A: Gas-electric network joint economic low-carbon dispatch optimization without considering dynamic gas network constraints.

Case B: Gas-electric network joint economic low-carbon dispatch optimization considering dynamic gas network constraints.

All parameters (network structure, storage tanks, generator units, power loads, fuel and gas prices) are identical in both cases. Optimization is performed with and without dynamic gas network flow/pressure constraints. Results are shown in Figures 21 and 22.

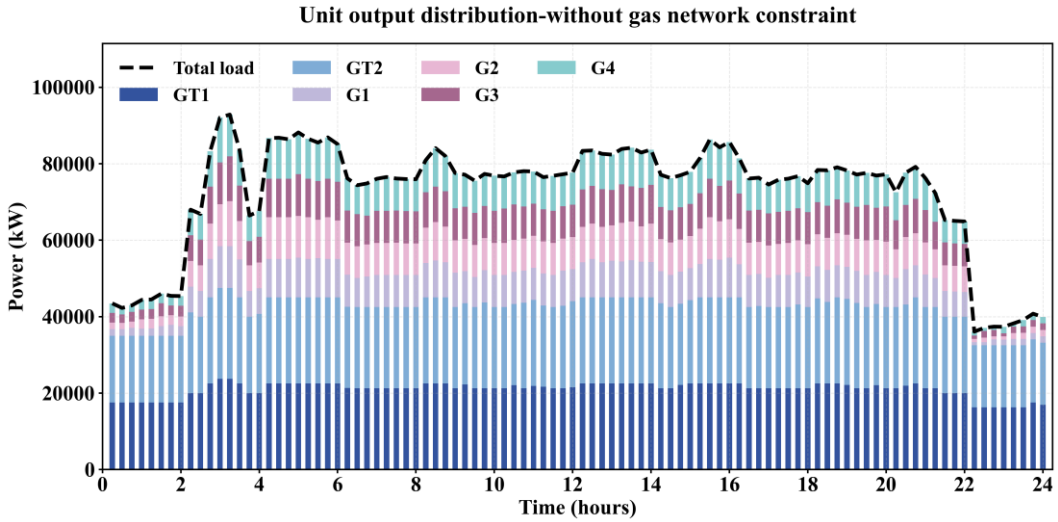



**Fig. 21** Output of each unit without gas network constraints

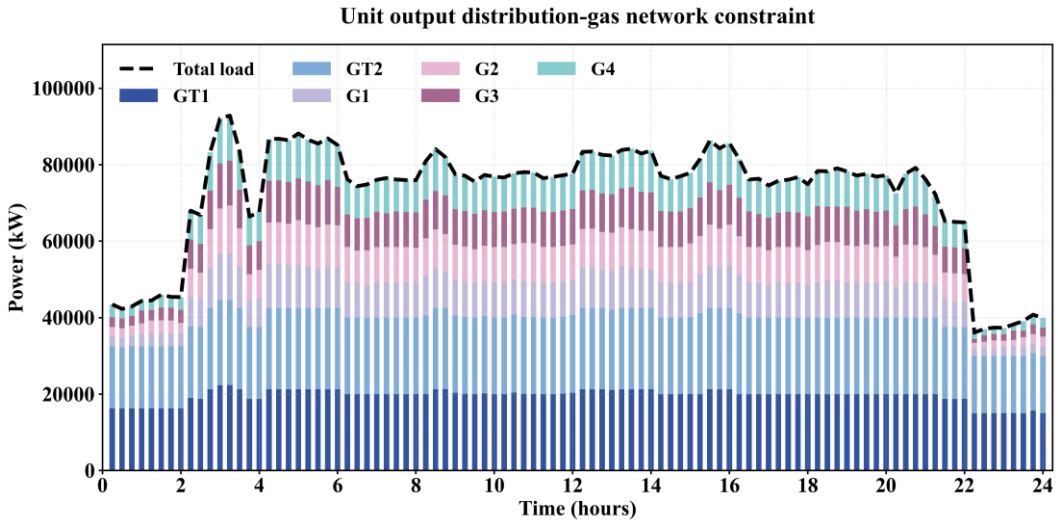



**Fig. 22** Output of each unit under gas network constraints

Simulation results show that dynamic gas-electric coupling significantly affects system operation. Without gas network constraints (Figure 21), gas-fired units GT1/GT2 (large capacity, low marginal cost, lower emissions) take base load; diesel units G1-G3 handle middle load; G4 covers peak load. As shown in Figure 23, total outputs: GT1 = 2,022,560.88 kWh, GT2 = 2,028,439.26 kWh; G1 = 725,687.77 kWh, G2 = 734,017.33 kWh, G3 = 733,063.32 kWh, G4 = 728,378.71 kWh. From cost and emission decomposition (Figures 24-25): gas-fired units – generation cost 164,616.68 USD, emission cost 36,248.21 USD, emissions 453,102.68 kg; diesel units – generation cost 122,142.76 USD, emission cost 39,727.60 USD, emissions 496,595.01 kg. Start-up/shut-down costs are zero. Diesel units have lower generation cost but higher emission cost and emissions, reflecting the Pareto trade-off between economy and low-carbon performance in multi-objective optimization.

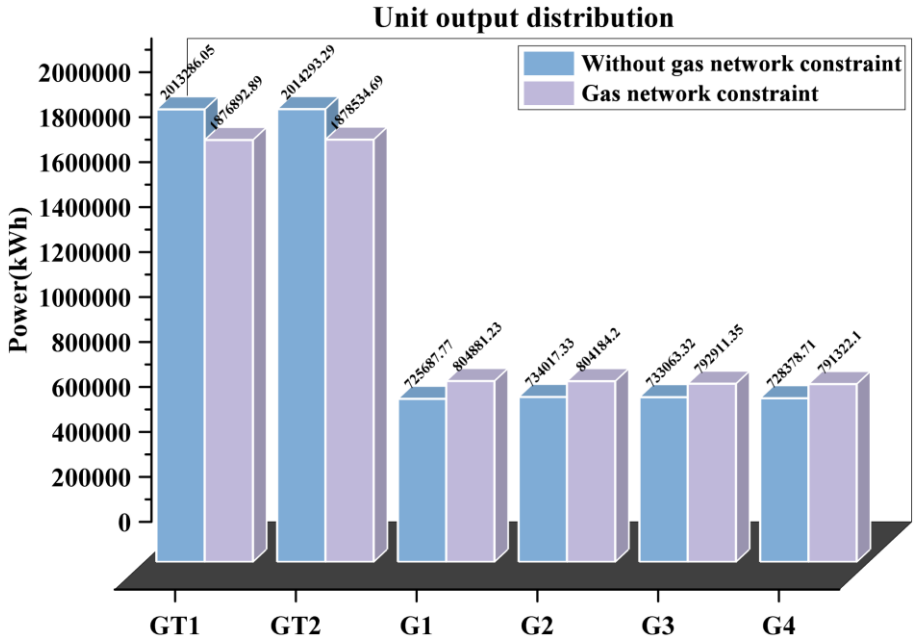



**Fig. 23** Total output of each unit with and without gas network constraints

When dynamic gas network constraints are applied (Figure 22), gas-fired unit operation changes significantly. Due to limited pipeline transmission capacity, the dynamic constraints tighten gas consumption upper limits via time-frequency iteration, reducing base load support. As shown in Figure 23, GT1 and GT2 outputs drop to 1,876,892.89 kWh and 1,878,534.69 kWh, respectively. To maintain power balance, diesel units G1-G4 increase output to 804,881.23, 804,184.20, 792,911.35, and 791,322.10 kWh, compensating for the deficit and handling middle/peak loads. Cost and emission decomposition (Figures 24-25) shows total system cost reduced by 1,462.69 USD. Gas-fired units: generation cost decreases to 149,506.75 USD, emission cost to 33,798.85 USD. Diesel units: generation cost increases to 134,538.11 USD, emission cost to 43,428.86 USD. Start-up/shut-down costs are zero. However, total system carbon emissions rise to 965,346.41 kg (gas-fired units: 422,485.60 kg; diesel units: 542,860.81 kg).

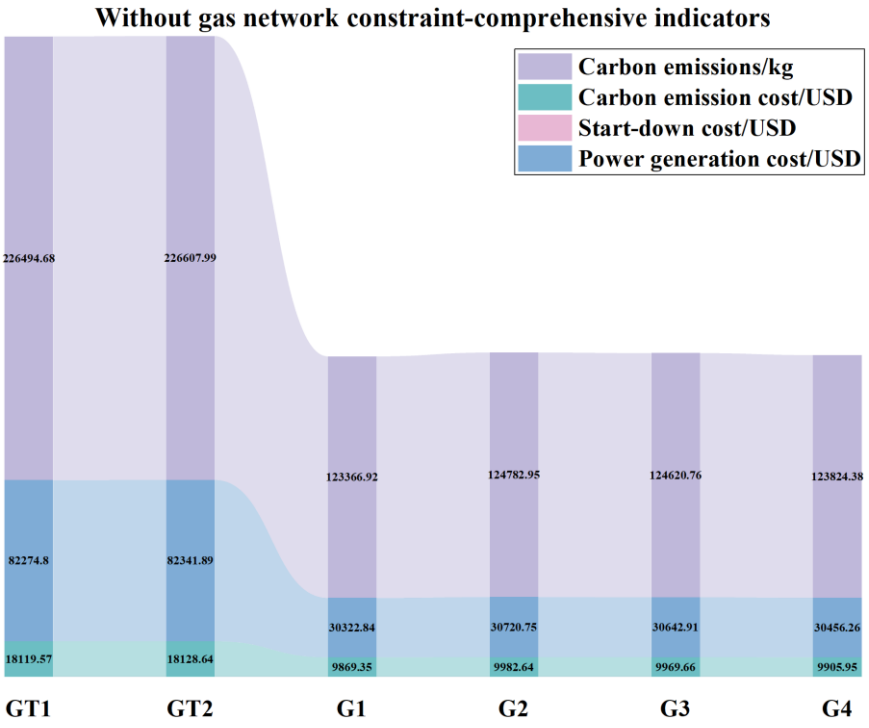



**Fig. 24** Comprehensive indicators of each unit without gas network constraints

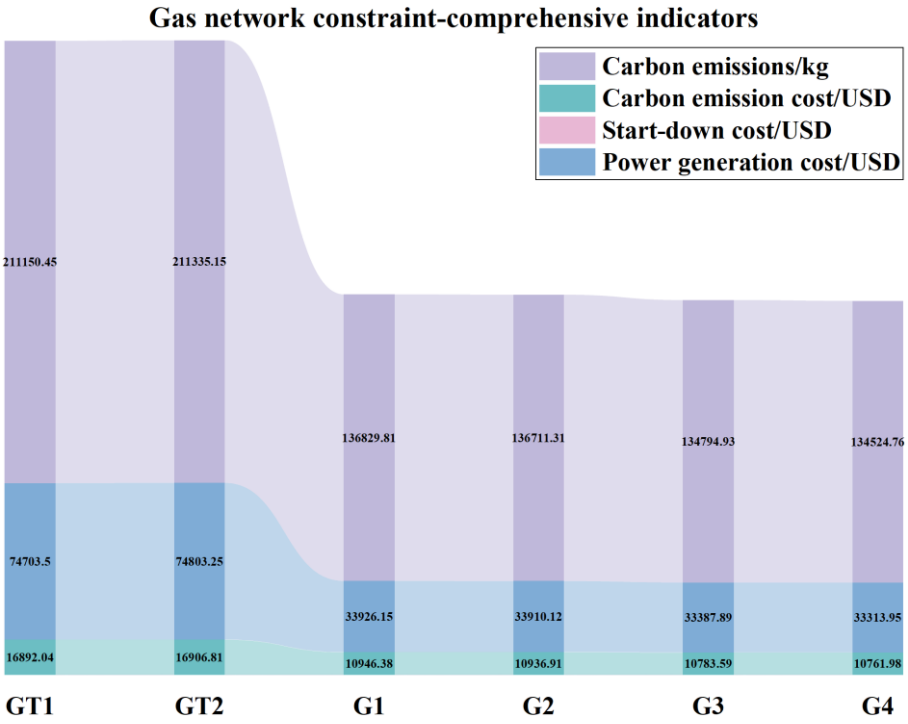


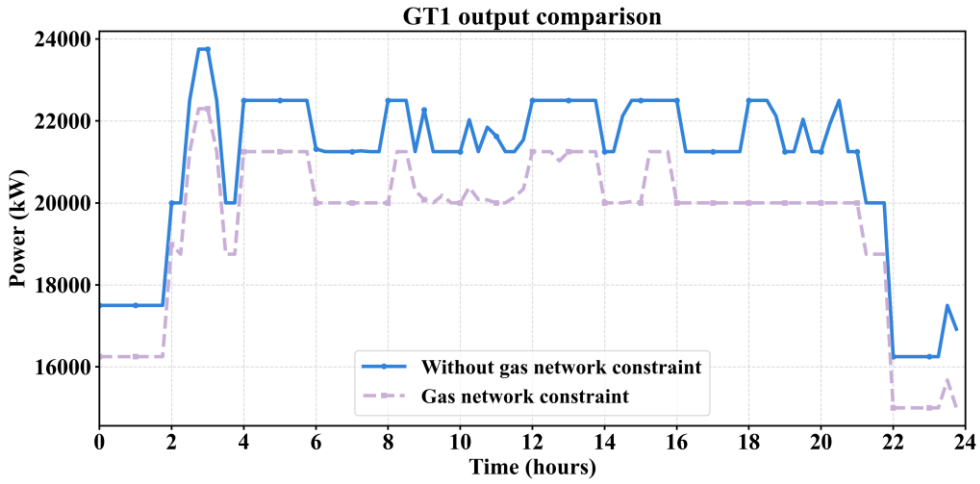

**Fig. 25** Comprehensive indicators of each unit under gas network constraints

Compared with the no-constraint scenario, gas-electric closed-loop constraints significantly alter energy allocation strategy. Gas-fired units GT1/GT2 output decrease by 6.77 and 6.74 %, while diesel units G1-G4 increase by 10.91, 9.56, 8.16, and 8.64 %, respectively. Total system cost drops by 0.4 %, but carbon emissions rise by 1.65 % - a Pareto trade-off. The driver is dynamic gas network constraints limiting gas-fired output, forcing diesel units to fill the gap (Figure 23). Gas-fired base-load support ratio falls from 57.96 to 54.04 %, while diesel regulation contribution rises from 42.04 to 45.96 %. This forms a two-stage "rigid constraint (gas-fired units cap)-flexible regulation (diesel unit compensation)" strategy, minimizing cost while ensuring ship reliability. These results lay the foundation for understanding the dynamic mechanisms behind macro-level improvements.

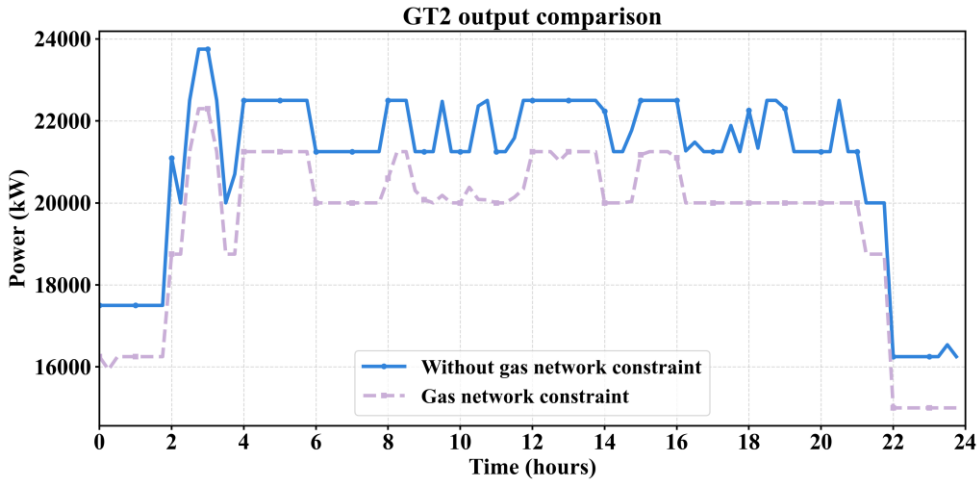
### 4.2.1 Electric network comparison analysis

To analyze the changes in power output of each gas-fired generator unit with and without gas network constraints, the results are shown in Figures 26 and 27.

Without gas network constraints (Figure 26), gas-fired units operate flexibly within 16,250~23,750 kW to meet base load. Diesel units (Figure 27) serve as flexible regulators for middle and peak loads. This indicates the model prioritizes gas-fired units for base-load operation to avoid start-up/shut-down costs, while flexibly dispatching diesel units to minimize total cost and emissions through coordinated output ratios, reflecting the collaborative optimization of the gas-electric coupling system.




(a)




(b)

**Fig. 26** Output comparison of gas-fired generators

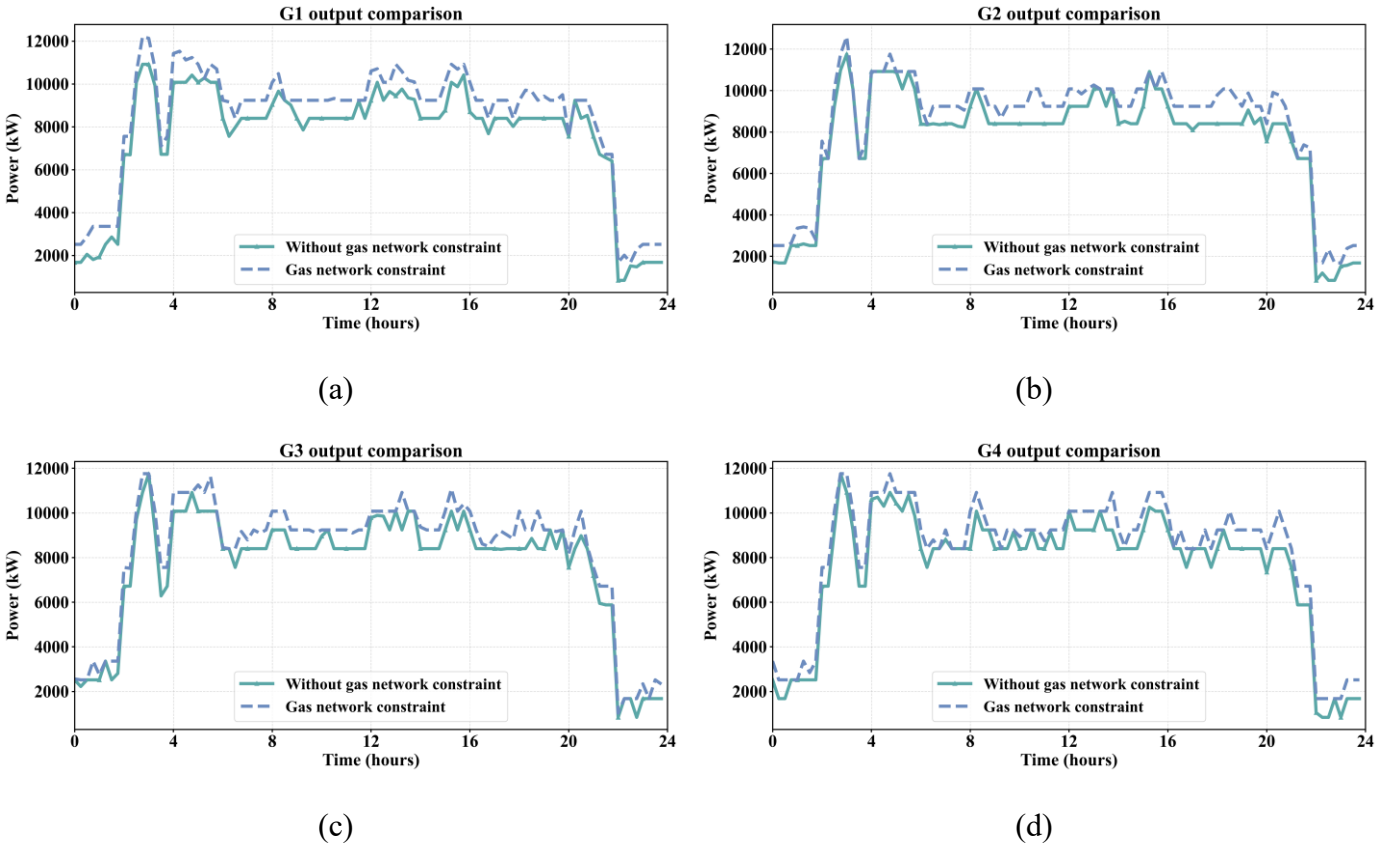



**Fig. 27** Output comparison of diesel generators

Under dynamic gas network constraints (Figure 26), gas-fired unit output is limited to 15,000~22,297 kW. From 2.5 h to 21 h, gas-fired units output stays above 20,000 kW (≥80 % efficiency). At other times, output adjusts with load and coordinates with diesel units to meet ship demand. Thus, the model prioritizes gas-fired units at efficient operating points while ensuring ship load. To optimize cost and emissions, it actively dispatches diesel units to fill the power gap from limited gas-fired units output, increasing diesel units dispatch frequency compared to the no-constraint scenario. This highlights gas-electric coupling: flexible diesel units regulation compensates for gas-fired unit limitations, enabling stable and safe system operation under gas network constraints.

### 4.2.2 Gas network comparison analysis

To analyze the microscopic changes of gas-fired units with and without gas network constraints, node flow variations are shown in Figures 28 and 29, and node pressure variations in Figures 30 and 31.

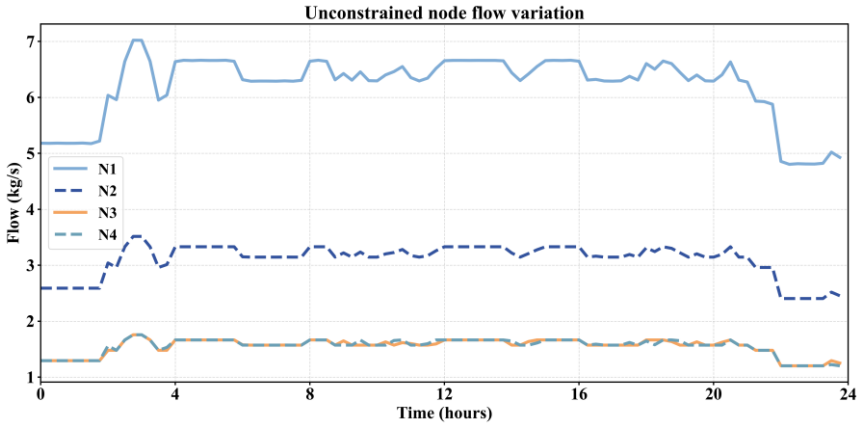



**Fig. 28** Node flow variation without gas network constraints

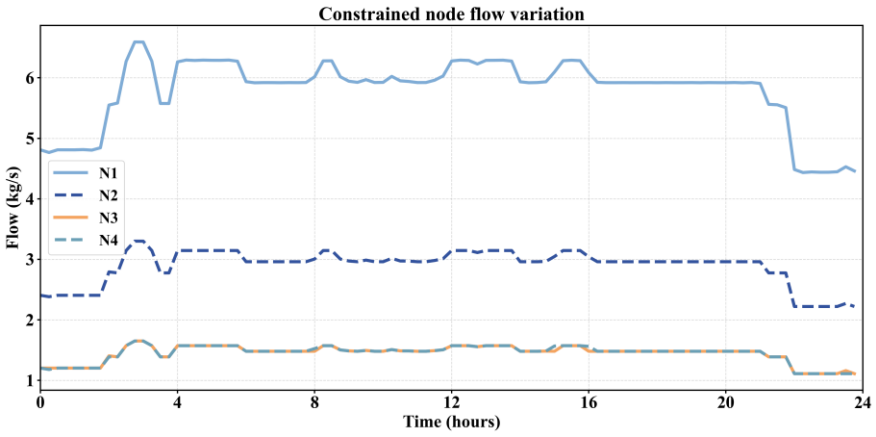



**Fig. 29** Node flow variation under gas network constraints

From the perspective of gas network node flow variations (Figures 28 and 29), the gas consumption trend at each node closely matches that of the corresponding gas-fired unit's power generation, reflecting the tight gas-electric coupling. Meanwhile, the supply flow at the gas source node slightly lags behind the consumption changes at the demand nodes, indicating a certain transmission delay in the gas network.

Without gas network constraints (Figure 28), the gas-fired units can flexibly consume gas within 1.2025~1.7575 kg/s for power generation, while gas supply node 1 varies accordingly within 4.8032~7.0204 kg/s, providing the system with significant operational flexibility.

In contrast, under dynamic gas network constraints (Figure 29), the total gas consumption of the gas-fired units ranges from 1.11 to 1.65 kg/s. Node 2, as a gas collecting node, varies within 2.22~3.3 kg/s according to the consumption at nodes 3 and 4. Constrained by the gas supply node, the gas-fired units' consumption remains stable at 1.48~1.65 kg/s during 8-21 h, yielding more stable and economic output compared with the unconstrained scenario. Since gas-consuming node 4 is closest to collecting node 2, its gas demand can be replenished fastest; thus GT2 can prioritize power output to meet the ship's electric load, further highlighting the important role of gas-electric coupling in dynamic system operation.

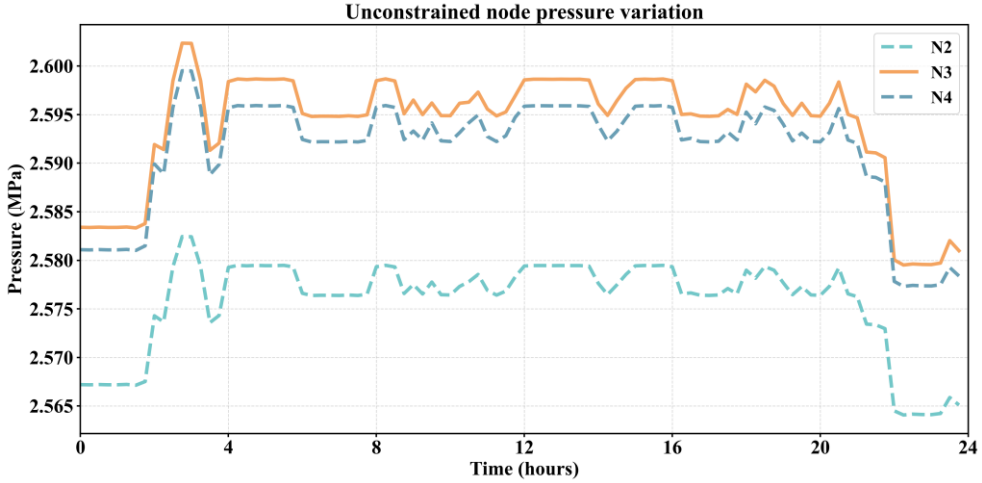



**Fig. 30** Node pressure variation without gas network constraints

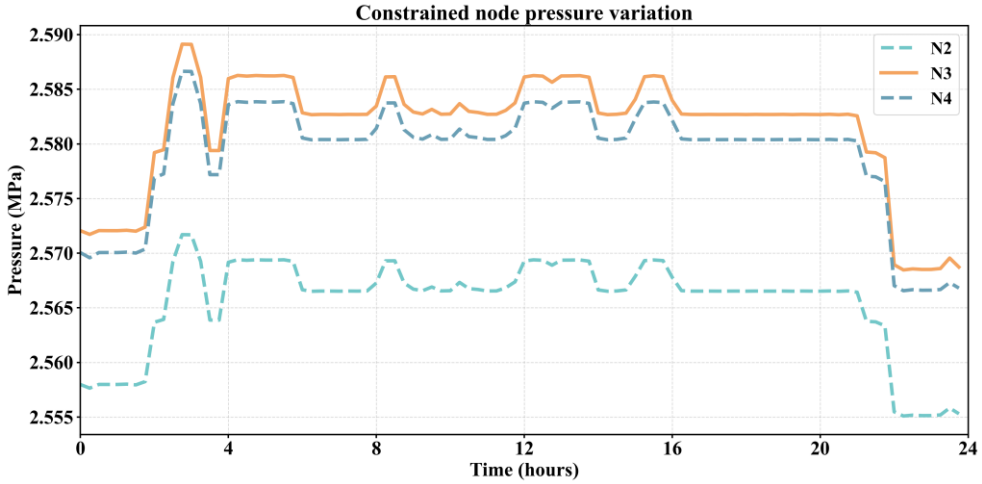



**Fig. 31** Node pressure variation under gas network constraints

From the perspective of gas network node pressure variations (Figures 30 and 31), with constant pressure at the gas source node, the pressure at each consuming node dynamically adjusts with the local gas flow change: increasing with higher consumption and decreasing with lower consumption. This reflects the tight flow-pressure coupling and the system's collaborative response mechanism. Specifically, the pressure changes rapidly at first and then gradually stabilizes, demonstrating the adaptive capability of the gas-electric coupling system.

Without gas network constraints (Figure 30), pressure fluctuations differ across nodes 2-4, with ranges of approximately 0.0184, 0.0228, and 0.0222 MPa, respectively. Node 2 exhibits the smallest fluctuation as it is closest to gas supply node 1, enabling the fastest replenishment and quickest pressure stabilization. This reflects both the gas network's transmission efficiency and the effective collaborative capability among nearby nodes.

Under gas network constraints (Figure 31), the pressure fluctuations further highlight the characteristics of gas-electric coupling, with ranges of approximately 0.0166, 0.0207, and 0.0201 MPa at nodes 2-4, respectively. Node 2 still shows the smallest fluctuation, while node 3 shows the largest due to its greatest distance from gas supply node 1, resulting in the longest replenishment time. As a collecting node, node 2's pressure closely follows the dynamic variations of nodes 3 and 4. During 8-21h, without gas network constraints, the considerable fluctuation in gas-fired units' consumption causes more pronounced pressure variations. In contrast, under gas supply node constraints, the stable consumption within 1.48~1.65 kg/s leads to relatively smooth pressure changes. This illustrates the response mechanism of the gas-electric coupling system under dynamic constraint variations and the differences in collaborative operation among nodes.

### 4.3 Case analysis of steady-state and dynamic gas network constraints

To quantitatively analyze the advantages of the dynamic gas network model over the steady-state model, two comparison scenarios are set up in this paper:

Scenario A adopts the dynamic gas network constraints based on time-frequency domain transformation, considering pipeline dynamic effects;

Scenario B adopts the steady-state gas network constraints based on the unified energy circuit theory [42], solved independently at each time step.

Both scenarios use the same gas-electric joint economic low-carbon dispatch model. Under identical power load, gas network topology, and physical constraints, the differences in economic cost, carbon emissions, and computational efficiency are compared via gas-electric closed-loop optimization. The unit outputs for the two scenarios are shown in Figures 32 and 33.

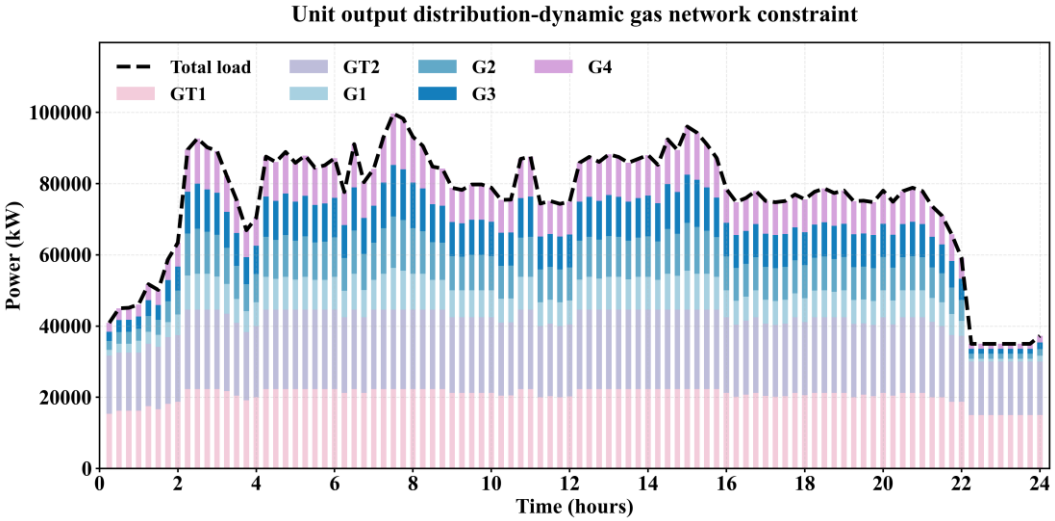



**Fig. 32** Output of each unit under dynamic gas network constraints

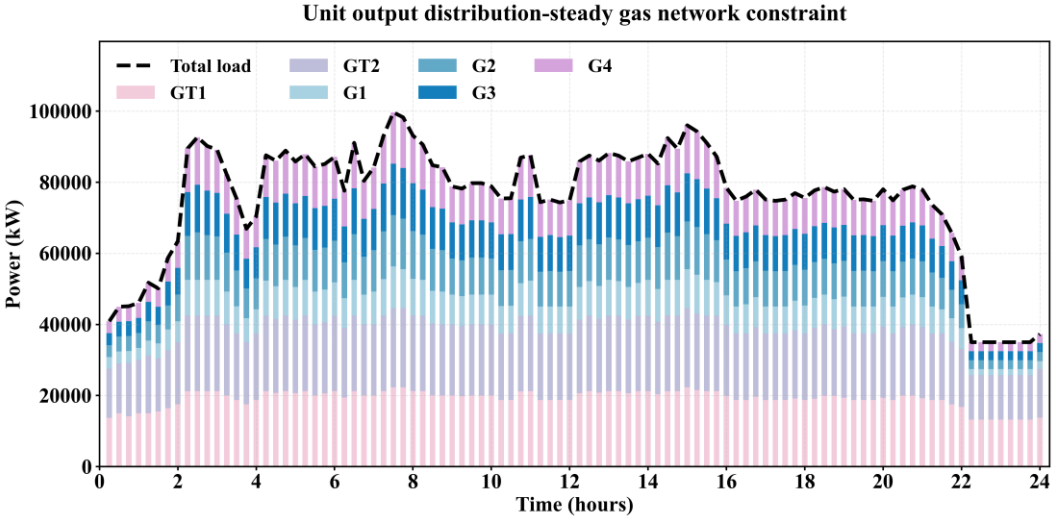
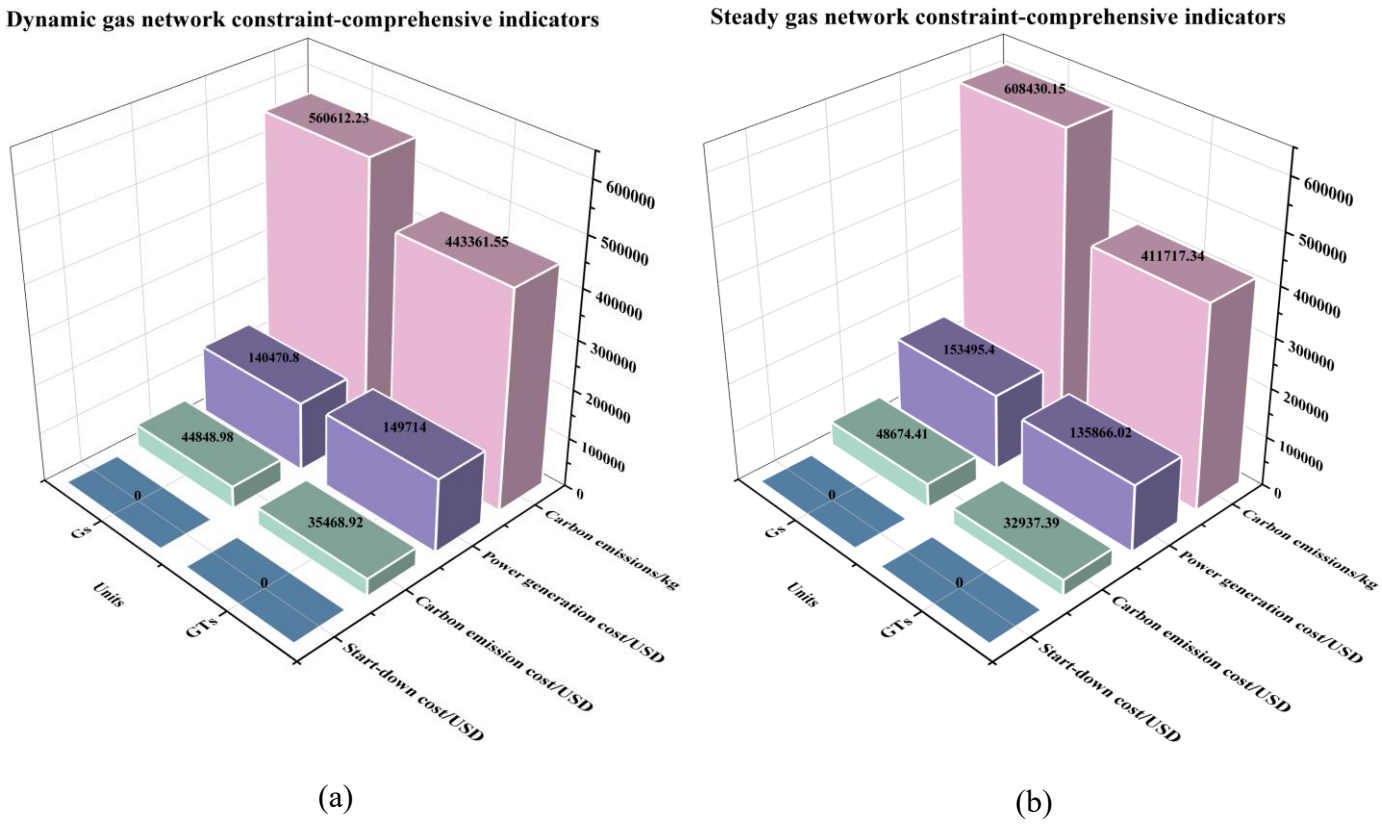



**Fig. 33** Output of each unit under steady-state gas network constraints

Under dynamic gas network constraints (Figure 32), the gas-fired units' total output reaches 3,940,991.59 kWh, accounting for 54.44 % of total generation. In contrast, under steady-state constraints (Figure 33), their output drops to 3,659,709.71 kWh (50.56 %). Correspondingly, the diesel units' share in the dynamic scenario is 45.56, 3.89 % lower than the steady-state scenario (49.44 %). This indicates that by considering the dynamic buffering effect of pipelines, the dynamic gas network model effectively expands the gas-fired units' output capacity, enabling more extensive utilization of the more economical gas-fired generation to substitute diesel power.




(a) (b)

**Fig. 34** Comprehensive indicators of each unit under dynamic and steady-state gas network constraints

Figure 34 compares the optimal operation results under dynamic and steady-state gas network constraints. The total cost under the dynamic scenario is 370,502.70 USD, 470.52 USD (0.13 %) lower than the steady-state scenario (370,973.22 USD). Although modest, this reduction reflects significant differences in unit output structures, revealing the unique advantages of the dynamic gas network model. From the cost composition: gas-fired generation cost is 149,714.00 USD, 13,847.99 USD higher than the steady-state scenario, while diesel generation cost is 140,470.80 USD, 13,024.61 USD lower. The comparable magnitude indicates a significant substitution effect of gas-fired for diesel power. Regarding carbon emission costs: gas-fired units emit 35,468.92 USD (2,531.54 USD higher), while diesel units emit 44,848.98 USD (3,825.43 USD lower). Overall, total carbon emission cost under the dynamic scenario is 80,317.90 USD, 1,293.90 USD lower than the steady-state scenario (81,611.80 USD). This demonstrates that by optimizing the generation structure and increasing the gas-fired share, the dynamic gas network model reduces total carbon emission cost while coordinating economy and environmental performance. In summary, the lower total cost under the dynamic scenario mainly results from the lower marginal cost and carbon emission advantage of gas-fired generation, along with improved overall system operating efficiency.

In terms of total carbon emissions (Figure 34), the dynamic gas network scenario emits 1,003,973.78 kg $CO_2$, 16,173.71 kg $CO_2$ (1.59 %) lower than the steady-state scenario (1,020,147.49 kg $CO_2$). This reduction stems from generation structure optimization: gas-fired units have lower carbon intensity, and the dynamic scenario achieves lower overall emissions by increasing their share. Specifically, gas-fired units emit 443,361.55 kg $CO_2$ (31,644.21 kg $CO_2$ higher), while diesel units emit 560,612.23 kg $CO_2$ (47,817.92 kg $CO_2$ lower). The greater decrease in diesel emissions than the increase in gas-fired emissions reflects the low-carbon benefit of substituting gas for diesel.

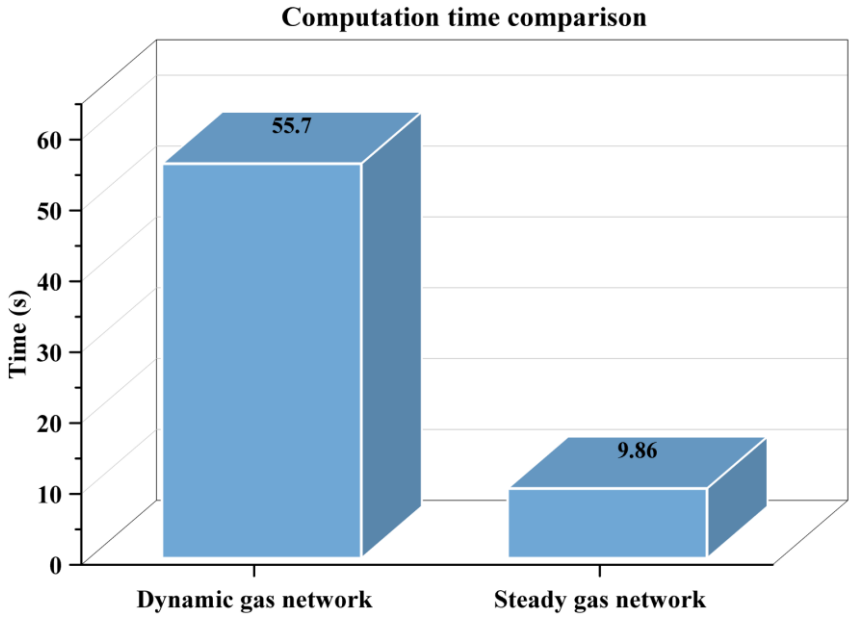



**Fig. 35** Comparison of computation time under dynamic and steady-state gas network constraints

In terms of computational efficiency (Figure 35), the dynamic gas network scenario requires 55.7 s, approximately 5.65 times the steady-state scenario (9.86 s). To identify the computational bottleneck of the dynamic model, we decomposed its total runtime of 55.7 s into four main modules, as summarized in Table 12.

The decomposition reveals that the MILP solution is the primary computational bottleneck, accounting for 63.2 % of the total time. This indicates that the time difference between the dynamic and steady-state models is primarily due to the increased MILP problem scale - the introduction of dynamic gas network constraints adds a large number of pressure- and flow-related constraints and variables - rather than the frequency-domain transformation per se, which together accounts for only 20.3 % of the total time. The closed-loop iteration overhead (16.5 %) is a non-negligible but secondary factor.

Although longer, the computation time remains acceptable for practical engineering applications. For day-ahead dispatch optimization (24-hour scheduling), 55.7 s is far below the dispatch horizon and meets practical requirements. From the trade-off perspective, the dynamic model achieves a 0.13 % cost reduction and 1.59% carbon emission reduction at the expense of 5.65 times the computation time - a reasonable trade-off under high carbon prices or stringent environmental requirements.

**Table 12** Computational time decomposition of the dynamic model

| Computation Module | Time (s) | Percentage |
|---|---|---|
| MILP solution (Gurobi) | 35.2 | 63.2 % |
| FFT/IFFT transformation | 4.8 | 8.6 % |
| Frequency-domain admittance matrix solution | 6.5 | 11.7 % |
| Closed-loop iteration overhead | 9.2 | 16.5 % |
| Total | 55.7 | 100 % |

### 4.3.1 Carbon price sensitivity analysis

To verify the robustness of the dynamic model's emission reduction advantage (1.59 % lower carbon emissions compared with the steady-state model under the baseline carbon price of 0.08 $/kg, we conducted a sensitivity analysis over a carbon price range of 0.04-0.12 $/kg (i.e., ±50 % around the baseline value). The results are summarized in Table 13.

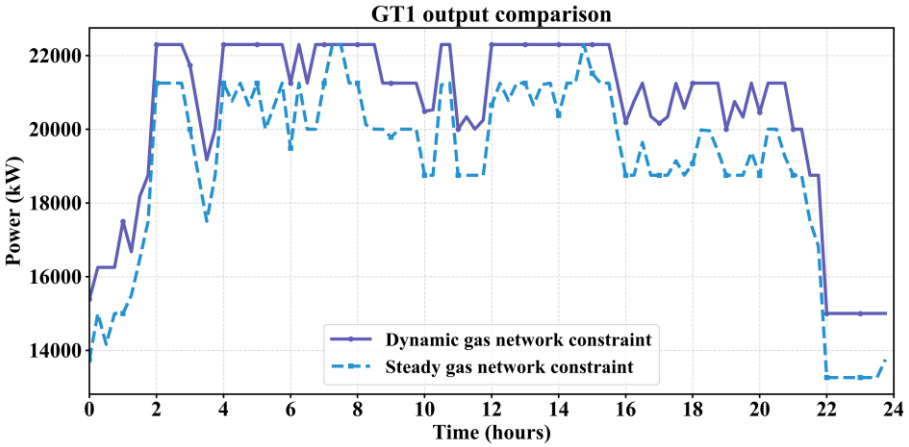
The sensitivity analysis reveals three important findings. First, the dynamic model consistently achieves 1.53-1.64 % emission reductions across the entire carbon price range. The baseline result of 1.59 %

lies near the centre of this interval, confirming that the emission reduction advantage is stable even under ±50 % carbon price fluctuations. Second, the cost reduction advantage of the dynamic model grows from 0.074 to 0.182 %, showing a monotonic increasing trend. This is because the dynamic model increases the share of gas-fired generation, which has a lower carbon intensity (approximately 66 % of diesel generators), yielding greater carbon cost savings when the carbon price is higher. Third, the dynamic model outperforms the steady-state model at all tested carbon price levels, confirming that the core conclusion is robust regardless of the specific carbon price selected.

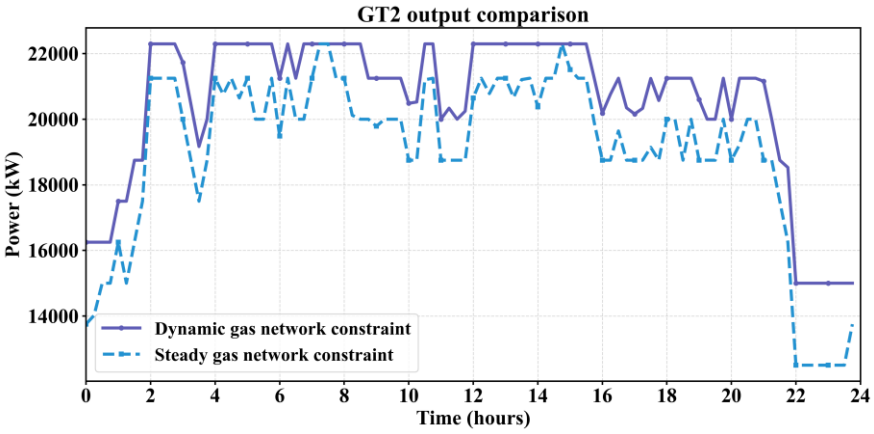
**Table 13** Carbon price sensitivity analysis results

| Carbon Price ($/kg) | Dynamic Model Total Cost ($) | Steady-State Model Total Cost ($) | Cost Reduction | Dynamic Model Emissions (kg) | Steady-State Model Emissions (kg) | Emission Reduction |
|---|---|---|---|---|---|---|
| 0.04 | 361,850 | 362,120 | 0.074 % | 1,054,200 | 1,071,800 | 1.64 % |
| 0.06 | 366,180 | 366,540 | 0.098 % | 1,029,100 | 1,045,900 | 1.61 % |
| **0.08** | **370,503** | **370,973** | **0.127 %** | **1,003,974** | **1,020,147** | **1.59 %** |
| 0.10 | 374,830 | 375,410 | 0.155 % | 978,900 | 994,400 | 1.56 % |
| 0.12 | 379,160 | 379,850 | 0.182 % | 953,800 | 968,600 | 1.53 % |

### 4.3.2 Electric network comparison analysis




(a)




(b)

**Fig. 36** Output comparison of gas-fired generators

From the detailed unit output perspective (Figure 36), GT1 and GT2 outputs in the dynamic gas network scenario are 1,969,362.09 kWh and 1,971,629.50 kWh, respectively - increases of 136,909.55 kWh (7.47 %) and 144,372.34 kWh (7.90 %) compared with the steady-state scenario. This directly reflects the full utilization of pipeline gas storage buffering capacity by the dynamic model.

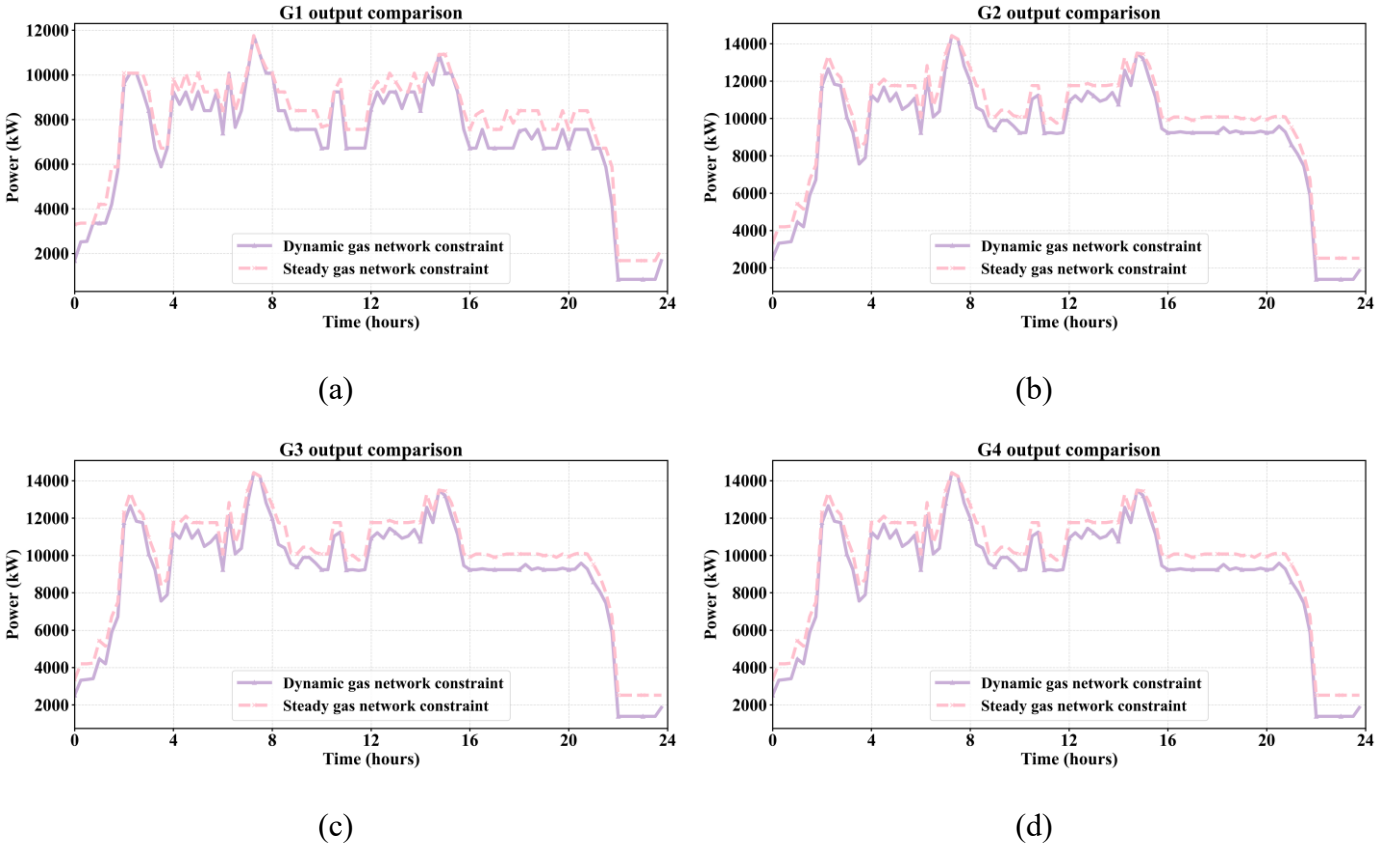



**Fig. 37** Output comparison of diesel generators

For diesel units (Figure 37), G3 outputs 684,594.54 kWh under the dynamic scenario, 67,481.22 kWh lower than the steady-state scenario, while G4-G6 each output 871,041.49 kWh, decreasing by 71,266.89 kWh per unit. This reduction indicates that the dynamic model, through more accurate pressure assessment, reduces the diesel reserve capacity required due to conservative gas network constraints.

Regarding unit operation stability, GT1 and GT2 power fluctuation rates in the dynamic scenario are 0.1111 and 0.1093, respectively - 13.6 and 19.75 % lower than the steady-state scenario (0.1286 and 0.1362). This reduction indicates that the dynamic model smooths gas-fired unit output fluctuations and improves operational stability. This is mainly attributed to the dynamic model accounting for gas inertial effects in pipelines, resulting in smoother pressure variations that enable gas-fired units to track load changes more stably and reduce unnecessary diesel unit output.

### 4.3.3 Gas network comparison analysis

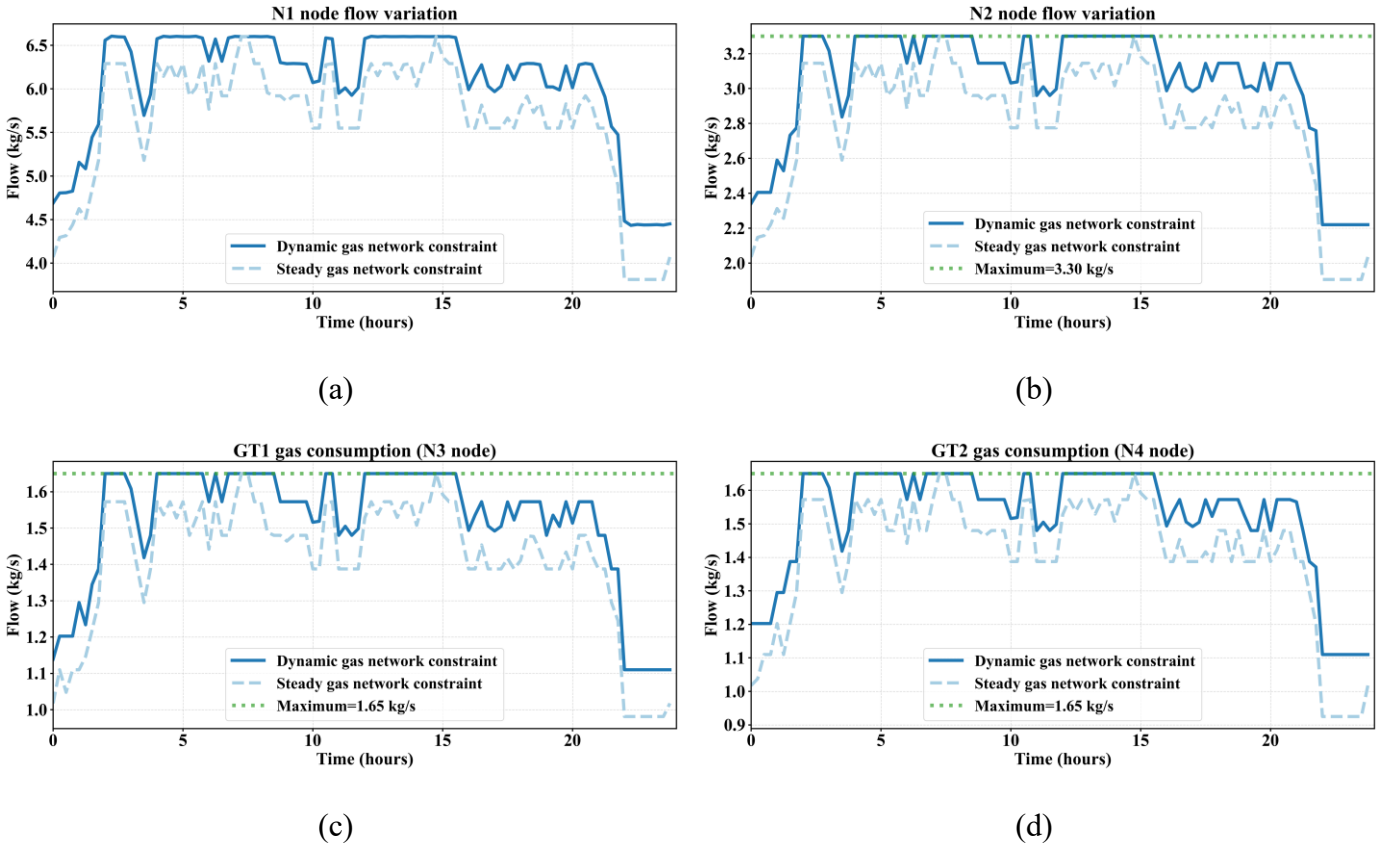



**Fig. 38** Comparison of node flows under dynamic and steady-state gas network constraints

To reveal operational differences under dynamic and steady-state gas network constraints, Figure 38 shows temporal flow variations at each node. Under the dynamic scenario, gas-fired unit consumption remains relatively high for most periods and frequently reaches the single-unit upper limit of 1.65 kg/s; under the steady-state scenario, consumption fluctuates more sharply and is noticeably lower during high-load periods. For GT1, the dynamic flow range is 1.1100~1.6500 kg/s (range 0.5400 kg/s), 0.1288 kg/s (19.26 %) lower than the steady-state range (0.9812~1.6500 kg/s, range 0.6688 kg/s); for GT2, the dynamic range of 0.5400 kg/s is 0.1850 kg/s (25.52 %) lower than the steady-state range of 0.7250 kg/s. This indicates that the dynamic model, by utilizing gas inertial effects and line pack buffering, avoids the frequent large adjustments required by the steady-state model, achieving smoother operation. Although both scenarios reach the maximum consumption limit, the dynamic scenario enables units to operate near the upper limit for more periods through smooth regulation, improving gas utilization efficiency.

The flow variation at converging node N2 also exhibits smoothing characteristics. Under the dynamic scenario, the N2 flow range is 2.2200~3.3000 kg/s (range 1.0800 kg/s), 0.3138 kg/s (22.51 %) lower than the steady-state scenario (1.9062~3.3000 kg/s, range 1.3938 kg/s). This helps reduce pipeline pressure pulsation and booster regulation burden; in contrast, severe flow fluctuations at N2 in the steady-state model may cause pressure violations, forcing dispatch to reserve more safety margins.

Gas supply at source node N1 is overall higher and fluctuates more gently under the dynamic scenario. The N1 flow range is 4.4335~6.6052 kg/s (range 2.1717 kg/s), 0.6158 kg/s (22.09 %) lower than the steady-state scenario (3.8125~6.6000 kg/s, range 2.7875 kg/s). The dynamic model maintains a higher baseline gas supply during low-load periods. The physical mechanism is that pipelines act as "energy storage devices": storing excess gas during low-load periods and releasing it during peak periods to buffer instantaneous demand, creating a "peak shaving and valley filling" effect. The steady-state model follows an "instantaneous balance" principle, forcing gas supply to drop to lower levels during low-load periods with severe fluctuations.

In summary, by exploiting the dynamic buffering effect of pipelines, the dynamic gas network model reduces flow fluctuations at each node by 19~26 %, significantly improving gas network operational stability. Flow smoothing creates favorable conditions for efficient gas-fired unit operation, while smoother gas supply demand reduces upstream system impact. This analysis verifies the advantages of the dynamic gas network model in optimal dispatch of gas-electric coupling systems at the micro level.

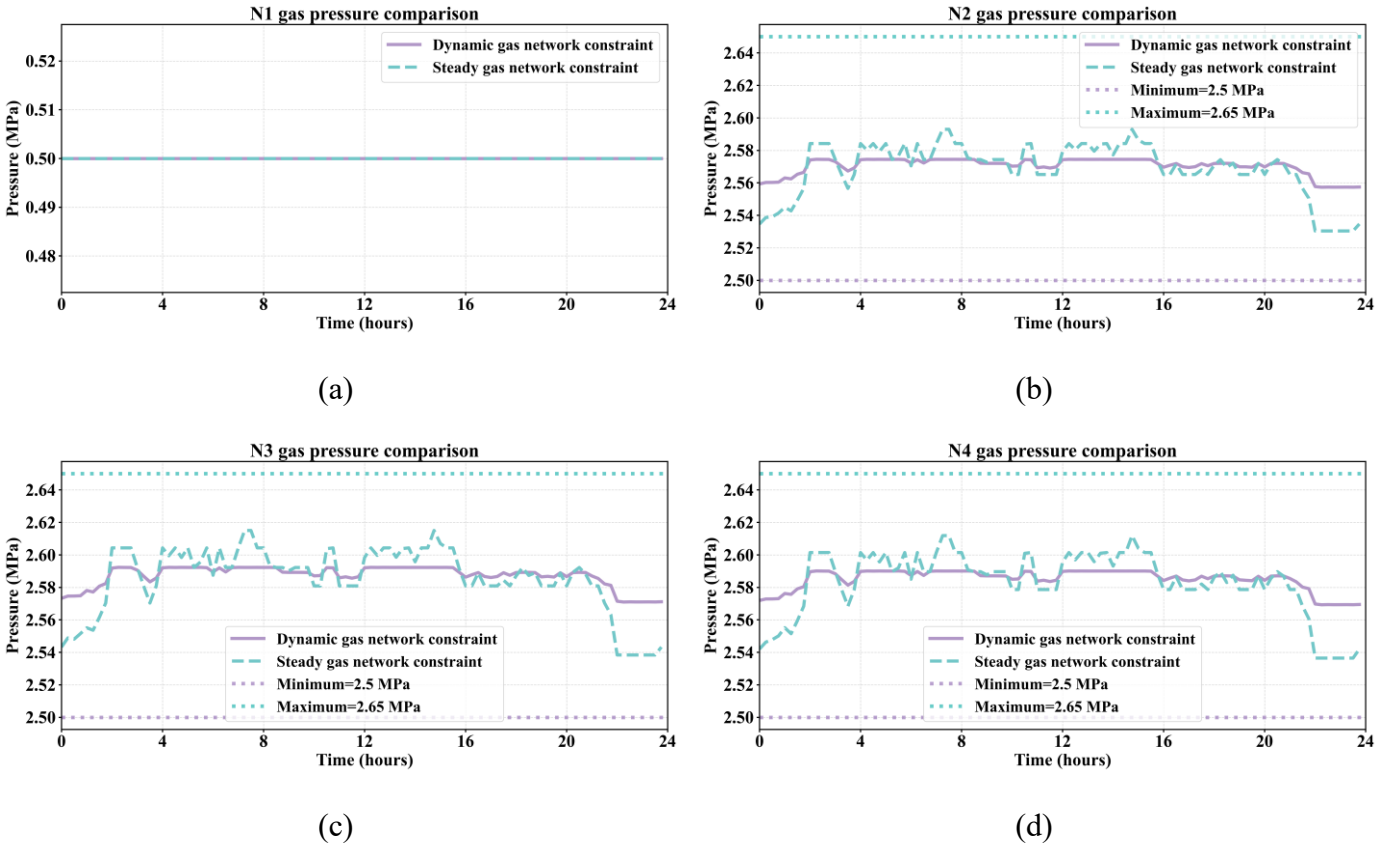



**Fig. 39** Comparison of node pressures under dynamic and steady-state gas network constraints

To reveal pressure characteristic differences under dynamic and steady-state gas network constraints, Figure 39 shows pressure time series at each node. Node N1 remains constant at 0.5 MPa in both scenarios, providing a unified baseline. At node N2 (booster outlet), pressure varies smoothly in the dynamic scenario, ranging 2.5573~2.5745 MPa (range 0.0172 MPa), while fluctuating severely in the steady-state scenario, ranging 2.5304~2.5930 MPa (range 0.0626 MPa). The dynamic range is reduced by 0.0454 MPa (72.52 %), attributed to the dynamic model's consideration of pipeline buffering effects that absorb upstream and downstream fluctuations, avoiding pressure oscillations amplified in the steady-state model by neglecting pipeline inertia. In the steady-state scenario, N2 pressure approaches the 2.65 MPa upper limit for some periods, increasing booster burden and even triggering protection. At nodes N3 and N4 (gas turbine inlets), similar patterns emerge: the dynamic range at N3 is 0.0214 MPa (2.5710~2.5924), 72.06 % lower than the steady-state range of 0.0766 MPa (2.5384~2.6150); at N4, the dynamic range of 0.0208 MPa is 72.41 % lower than the steady-state range of 0.0754 MPa. Gas turbines are sensitive to inlet pressure fluctuations; the dynamic model provides a more stable operating environment, benefiting efficient combustion and extending service life. Regarding safety margins, the dynamic scenario maintains 0.0576 MPa from the upper limit and 0.0710 MPa from the lower limit at N3, both larger than the steady-state scenario (0.0350 and 0.0384 MPa). Thus, the dynamic model allows higher gas turbine output while maintaining larger safety margins, demonstrating its advantage of "balancing safety and efficiency."

Considering all nodes, the dynamic model reduces pressure fluctuation amplitude by about 72 %, significantly improving operational stability. The mechanism lies in the time-frequency domain method accurately capturing pressure wave propagation attenuation caused by gas compressibility and inertia, whereas

the steady-state model assumes instantaneous, non-attenuating propagation, amplifying pressure changes. Pressure smoothing directly translates into increased gas turbine output capacity, while synchronized variations at N2, N3, and N4 validate the dynamic model's physical plausibility. Moreover, high-frequency pressure fluctuations accelerate pipeline fatigue and valve wear; by reducing such fluctuations, the dynamic model helps extend equipment life and reduce life-cycle costs.

To quantitatively support the micro-level comparison between the dynamic and steady-state models, statistical summaries of nodal pressure fluctuations, branch flow fluctuations, and gas turbine power fluctuations are presented in Tables 14-16.

**Table 14** Comparison of nodal pressure fluctuations under dynamic and steady-state models

| Node | Dynamic model pressure range (MPa) | Dynamic model fluctuation amplitude (MPa) | Steady-state model pressure range (MPa) | Steady-state model fluctuation amplitude (MPa) | Amplitude reduction |
|---|---|---|---|---|---|
| N1 | 0.5000 | 0 | 0.5000 | 0 | — |
| N2 | 2.5573-2.5745 | 0.0172 | 2.5304-2.5930 | 0.0626 | 72.52 % |
| N3 | 2.5710-2.5924 | 0.0214 | 2.5384-2.6150 | 0.0766 | 72.06 % |
| N4 | 2.5682-2.5890 | 0.0208 | 2.5356-2.6110 | 0.0754 | 72.41 % |

**Table 15** Comparison of branch flow fluctuations under dynamic and steady-state model

| Branch | Dynamic model flow range (kg/s) | Dynamic model fluctuation amplitude (kg/s) | Steady-state model flow range (kg/s) | Steady-state model fluctuation amplitude (kg/s) | Amplitude reduction |
|---|---|---|---|---|---|
| GT1 (N3) | 1.1100-1.6500 | 0.5400 | 0.9812-1.6500 | 0.6688 | 19.26 % |
| GT2 (N4) | 1.1100-1.6500 | 0.5400 | 0.9250-1.6500 | 0.7250 | 25.52 % |
| N2 (collector) | 2.2200-3.3000 | 1.0800 | 1.9062-3.3000 | 1.3938 | 22.51 % |
| N1 (source) | 4.4335-6.6052 | 2.1717 | 3.8125-6.6000 | 2.7875 | 22.09 % |

**Table 16** Comparison of gas turbine power fluctuations under dynamic and steady-state models

| Unit | Dynamic model power range (kW) | Dynamic model fluctuation rate | Steady-state model power range (kW) | Steady-state model fluctuation rate | Fluctuation rate reduction |
|---|---|---|---|---|---|
| GT1 | 15,000-22,297 | 0.1111 | 16,250-23,750 | 0.1286 | 13.6 % |
| GT2 | 15,000-22,297 | 0.1093 | 16,250-23,750 | 0.1362 | 19.8 % |

Table 14 shows that the dynamic model reduces nodal pressure fluctuation amplitudes by approximately 72 % across all nodes, with Node 2 (closest to the gas source) exhibiting the smallest fluctuation and Node 3 (farthest from the source) exhibiting the largest. Table 15 demonstrates that branch flow fluctuation amplitudes are reduced by 19-26 % under the dynamic model. The dynamic model maintains a higher baseline gas supply during low-load periods (N1 minimum flow: 4.43 vs. 3.81 kg/s for the steady-state model), reflecting the pipeline 'energy storage' effect - pipelines store excess gas during low-load periods and release it during peak periods, smoothing the supply demand. Table 16 shows that the gas turbine power fluctuation rates are reduced by 13.6-19.8 %, indicating more stable unit operation and extended equipment life. These quantitative results confirm the advantages of the dynamic model at the micro-level of the gas network.

In summary, the pressure analysis verifies the dynamic model's advantages: by accurately accounting for pipeline dynamic characteristics, it achieves significant pressure smoothing, creates favorable conditions for efficient and stable gas turbine operation, and improves gas network equipment safety and service life.

The reduction in pressure fluctuations is interrelated with flow smoothing, together forming the theoretical basis for the economic and low-carbon advantages of the dynamic gas network model.

## 5. Conclusion

This paper proposes a dynamic natural gas network model and a joint economic low carbon dispatch framework for hybrid ships. Key conclusions:

1. The dynamic natural gas network model is efficient and accurate. The time frequency domain model reduces PDEs to algebraic equations, computing in 2.14 s (8 iterations) - 4.6× faster than finite difference (9.89 s) and 3.7× faster than finite element (7.9 s). Mean absolute errors: $1.29\times10^{-4}$ kg/s (flow) and $1.24\times10^{-4}$ MPa (pressure). On a 7 node network, speedup reaches 5.3×, confirming scalability.

2. Dynamic gas network constraints significantly improve dispatch strategies and economy. With dynamic constraints, gas fired units GT1/GT2 output drop by 6.77 and 6.74 %, diesel units G1-G4 increase by 8.16~10.91 %. Total cost decreases 0.4 %, emissions rise 1.65 % - a Pareto trade off.

3. Under dynamic gas network constraints, the gas-electric coupling system achieves "rigid constraint–flexible regulation" collaborative control. The dynamic model enables a two stage "rigid constraint (gas consumption cap)-flexible regulation (diesel backup) " strategy, minimizing cost while ensuring reliability.

4. The dynamic model shows significant comprehensive advantages over the steady-state model. Dynamic model increases gas fired share by 3.89 %, reduces cost by 0.13 %, cuts emissions by 1.59 %, lowers gas unit power fluctuation by 13.6~19.8 %, decreases node pressure fluctuation by about 72 % and node flow fluctuation by 19~26 %. Computation time is 55.7 s (5.65× steady state) but meets day ahead dispatch needs.

In summary, the method accurately captures gas network dynamics, coordinates gas and diesel units, reduces cost and emissions while ensuring stability, and provides theoretical and technical support for hybrid power ship applications.

## NOMENCLATURE

| Category | Symbol | Description | Domain |
|---|---|---|---|
| Gas properties | $\rho$ | Gas density | Time |
| Gas properties | $v$ | Gas flow velocity | Time |
| Gas properties | $p$ | Gas pressure | Time |
| Gas properties | $G$ | Gas mass flow rate | Time |
| Gas properties | $T$ | Gas temperature | Time |
| Pipeline geometry | $D$ | Inner diameter | — |
| Pipeline geometry | $A$ | Cross-sectional area | — |
| Pipeline geometry | $L$ | Pipeline length | — |
| Pipeline geometry | $\lambda$ | Friction coefficient | — |
| Pipeline geometry | $\theta$ | Pipeline inclination angle | — |
| Gas circuit components | $R_g$ | Gas resistance ($\lambda v_b/(AD)$) | Time |
| Gas circuit components | $L_g$ | Gas inductance ($1/A$) | Time |
| Gas circuit components | $C_g$ | Gas capacitance ($A/(RT)$) | Time |
| Gas circuit components | $k_g$ | Controlled gas pressure source coefficient | Time |
| Gas circuit components | $E_b$ | Pressure source (compressor boost) | Time |
| Gas circuit components | $y_b$ | Branch admittance | Frequency |
| Frequency-domain variables | $\tilde{G}(x,\omega)$ | Fourier transform of gas flow rate | Frequency |

| | | | |
|---|---|---|---|
| Frequency-domain variables | $\tilde{p}(x,\omega)$ | Fourier transform of gas pressure | Frequency |
| Frequency-domain variables | $\mathbf{Y}_g^{\omega}$ | Node admittance matrix in frequency domain | Frequency |
| Frequency-domain variables | $\dot{\boldsymbol{p}}_g^{\omega}$ | Nodal pressure phasor vector | Frequency |
| Frequency-domain variables | $\dot{\boldsymbol{G}}_g^{\omega}$ | Nodal gas injection phasor vector | Frequency |
| Network matrices | $A_g$ | Node-branch incidence matrix | — |
| Network matrices | $A_{g+}$ | Node outflow branch correlation matrix | — |
| Network matrices | $A_{g-}$ | Node inflow branch correlation matrix | — |

## FUNDING

This work is supported by "Research on Comprehensive Test and Verification of Intelligent Ships".

## REFERENCES

[1] Kondratenko, A.A., Zhang, M., Tavakoli, S., 2025. Existing technologies and scientific advancements to decarbonize shipping by retrofitting. *Renewable and Sustainable Energy Reviews*, 212, 115430. https://doi.org/10.1016/j.rser.2025.115430

[2] Wang, Z., Liao, P., Long, F., 2025. Maritime electrification pathways for sustainable shipping: Technological advances, environmental drivers, challenges, and prospects. *eTransportation*, 26, 100462. https://doi.org/10.1016/j.etran.2025.100462

[3] Al Baity, O.A., Ahmed, Y.M., ElGohary, M.M., 2026. Hybrid marine power systems: techno-economic and environmental optimisation of alternative fuel pathways. *Brodogradnja*, 77(3), 77304. https://doi.org/10.21278/brod77304

[4] Ammar, N.R., Seddiek, I.S., 2025. Enhancing sustainability in LNG carriers through integrated alternative propulsion systems with flettner rotor assistance. *Brodogradnja*, 76(1), 76102. https://doi.org/10.21278/brod76102

[5] Wen, J., Lu, J., Zhang, S., 2024. Intelligent control for rapidity and security of all-electric ships gas turbine under complex mutation load using optimized neural network. *Applied Thermal Engineering*, 248, 123120. https://doi.org/10.1016/j.applthermaleng.2024.123120

[6] Marfatia, Z., Li, X., 2022. On steady state modelling for optimization of natural gas pipeline networks. C*hemical Engineering Science,* 255, 117636. https://doi.org/10.1016/j.ces.2022.117636

[7] Ganter, S., Martini, T., Kopustinskas, V., 2024. A highly robust gas network simulation approach through an inherently solvable problem formulation for network states far from intended design points. *Applied Mathematical Modelling*, 127, 297-326. https://doi.org/10.1016/j.apm.2023.12.009

[8] Yang, J., Zhang, N., Botterud, A., 2020. Situation awareness of electricity-gas coupled systems with a multi-port equivalent gas network model. *Applied Energy*, 258, 114029. https://doi.org/10.1016/j.apenergy.2019.114029

[9] Farzaneh-Gord, M., Rahbari, H.R., 2016. Unsteady natural gas flow within pipeline network, an analytical approach. *Journal of Natural Gas Science and Engineering*, 28, 397-409. https://doi.org/10.1016/j.jngse.2015.12.017

[10] Li, X., Zhao, T., Sun, Q.H., 2022. Frequency response function method for dynamic gas flow modeling and its application in pipeline system leakage diagnosis. *Applied Energy*, 324, 119720. https://doi.org/10.1016/j.apenergy.2022.119720

[11] Dzedzemane, R., Wiid, A.J., Le Roux, J.D., 2024. Natural gas well production network state-space model development and validation for process control. *Industrial & Engineering Chemistry Research*, 63(3), 1461-1473. https://doi.org/10.1021/acs.iecr.3c00990

[12] Fakhroleslam, M., Bozorgmehry Boozarjomehry, R., Sahlodin, A.M., 2021. Dynamic simulation of natural gas transmission pipeline systems through autoregressive neural networks. *Industrial & Engineering Chemistry Research*, 60(27), 9851-9859.https://doi.org/10.1021/acs.iecr.1c00802

[13] Gao, H., Li, Z., Wang, C., 2023. Rolling dispatch framework of integrated electricity-gas system considering power-to-gas facilities and natural gas network dynamics: Modelling and case studies. *International Journal of Electrical Power & Energy Systems*, 152, 109259. https://doi.org/10.1016/j.ijepes.2023.109259

[14] Bayani, R., Manshadi, S.D., 2023. Coordinating flexible ramping products with dynamics of the natural gas network. *Sustainable Energy, Grids and Networks*, 35, 101079. https://doi.org/10.1016/j.segan.2023.101079

[15] Huang, Y., Feng, L., 2023. An Equivalent Dynamic Gas Network Model with Electricity-Gas Systems. *Industrial & Engineering Chemistry Research*, 62(30), 11905-11916. https://doi.org/10.1021/acs.iecr.3c01276

[16] Wen, K., Jiao, J., Zhao, K., 2023. Rapid transient operation control method of natural gas pipeline networks based on user demand prediction. *Energy*, 264, 126093. https://doi.org/10.1016/j.energy.2022.126093

[17] Zhou, D., Wang, C., Yan, S., 2022. Dynamic modeling and characteristic analysis of natural gas network with hydrogen injections. *International Journal of Hydrogen Energy*, 47(78), 33209-33223. https://doi.org/10.1016/j.ijhydene.2022.07.246

[18] Zhang, B., Xu, N., Zhang, H., 2024. Influence of hydrogen blending on the operation of natural gas pipeline network considering the compressor power optimization. *Applied Energy*, 358, 122594. https://doi.org/10.1016/j.apenergy.2023.122594

[19] Arya, A.K., Katiyar, R., Kumar, P.S., 2023. A multi-objective model for optimizing hydrogen injected-high pressure natural gas pipeline networks. *International Journal of Hydrogen Energy*, 48(76), 29699-29723. https://doi.org/10.1016/j.ijhydene.2023.04.133

[20] Wang, Z., Liao, P., Liu, S., 2025. Scenario-based energy management optimization of hydrogen-electric-thermal systems in sustainable shipping. *International Journal of Hydrogen Energy*, 99, 566-578. https://doi.org/10.1016/j.ijhydene.2024.12.070

[21] Liu, H., Fan, A., Li, Y., 2025. Multi-objective hierarchical energy management strategy for fuel cell/battery hybrid power ships. *Applied energy*, 379, 124981. https://doi.org/10.1016/j.apenergy.2024.124981

[22] Zhang, Y., Xue, Q., Gao, D., 2022. Two-level model predictive control energy management strategy for hybrid power ships with hybrid energy storage system. *Journal of Energy Storage*, 52, 104763. https://doi.org/10.1016/j.est.2022.104763

[23] Pang, B., Liu, S., Zhu, H., 2024. Real-time optimal control of an LNG-fueled hybrid electric ship considering battery degradations. *Energy*, 296, 131170. https://doi.org/10.1016/j.energy.2024.131170

[24] Si, Y., Wang, R., Zhang, S., 2022. Configuration optimization and energy management of hybrid energy system for marine using quantum computing. *Energy*, 253, 124131. https://doi.org/10.1016/j.energy.2022.124131

[25] Ouyang, T., Qin, P., Tuo, X., 2025. Low-carbon economic scheduling of large ship power system based on multi-energy cooperative utilization. *Energy*, 314, 134242. https://doi.org/10.1016/j.energy.2024.134242

[26] Ganjian, M., Farahabadi, H.B., Firuzjaei, M.R., 2024. Voyage scheduling and energy management co-optimization in hydrogen-powered ships. *International Journal of Hydrogen Energy*, 86, 788-799. https://doi.org/10.1016/j.ijhydene.2024.08.428

[27] Wang, X., Zhu, H., Luo, X., 2024. A novel optimal dispatch strategy for hybrid energy ship power system based on the improved NSGA-II algorithm. *Electric Power Systems Research*, 232, 110385. https://doi.org/10.1016/j.epsr.2024.110385

[28] Wang, X., Zhu, H., Luo, X., Chang, S., Guan, X. (2025) Improved Differential Mutation Aquila Optimizer-Based Optimization Dispatching Strategy for Hybrid Energy Ship Power System. *IEEE Transactions on Transportation Electrification*, 11(5), 12667-12683. https://doi.org/10.1109/TTE.2025.3593366

[29] Lu, D., Wang, A., Gan, H., Su, Y., Ao, X., 2025. A multi-objective collaborative optimization method of ship energy efficiency based on NSGA-II and TOPSIS. *Brodogradnja*, 76(3), 76301. https://doi.org/10.21278/brod76301

[30] Bortuzzo, V., Bertagna, S., Braidotti, L., 2025. An innovative tool for the evaluation of energy efficiency of merchant ships. *Brodogradnja*, 76(3), 76304. https://doi.org/10.21278/brod76304

[31] Najjaran, S., Skjetne, R., 2025. Nested optimal energy scheduling and power allocation for zero-emission high-speed passenger vessels. *Ocean Engineering*, 322, 120223. https://doi.org/10.1016/j.oceaneng.2024.120223

[32] Yang, Q., Zhang, S., Zhao, W., 2025. A two-stage energy management strategy for hybrid ship power systems considering the dynamic output characteristics of batteries. *Applied Energy*, 396, 126232. https://doi.org/10.1016/j.apenergy.2025.126232

[33] Wang, X., Li, Z., Luo, X., 2024. A Bi-level optimization dispatch for hybrid shipboard microgrid considering electricity-gas-heat coupling. *Green Energy and Resources*, 2(2), 100070. https://doi.org/10.1016/j.gerr.2024.100070

[34] Ren, Y., Zhang, L., Shi, P., 2022. Research on multi-energy integrated ship energy management system based on hierarchical control collaborative optimization strategy. *Journal of Marine Science and Engineering*, 10(10), 1556. https://doi.org/10.3390/jmse10101556

[35] Liao, W., Xiao, L., Zhang, F., 2022. Research on control strategy of a multi-energy ship microgrid using diesel-battery rotation. *Energy Reports*, 8, 13948-13958. https://doi.org/10.1016/j.egyr.2022.10.335

[36] Bao, K., Hu, L., 2024. Research on static security analysis and assessment method of integrated energy systems based on the unified energy circuit theory. *Journal of Physics: Conference Series*, 2917(1), 012004. https://doi.org/10.1088/1742-6596/2917/1/012004

[37] Chen, H., Wang, Z., Lin, Y., 2021. Optimal Dispatch of Integrated Energy System Based on Unified Energy Path Theory. *5th International Conference on Power and Energy Engineering* (ICPEE), 2-4 December, Xiamen, China, 181-188. https://doi.org/10.1109/ICPEE54380.2021.9662562

[38] Sun, Q., Dong, Q., You, S., 2020. A unified energy flow analysis considering initial guesses in complex multi-energy carrier systems. *Energy*, 213, 118812. https://doi.org/10.1016/j.energy.2020.118812

[39] Luo J., Xu N., Zhao S., 2019. Unified Energy Flow Analysis in Integrated Energy Systems Considering Nonlinear Performance. *2019 IEEE 2nd International Conference on Automation, Electronics and Electrical Engineering* (AUTEEE), 22-24 November, Shenyang, China, 88-93. https://doi.org/10.1109/AUTEEE48671.2019.9033301

[40] Song, J., Wang, Y., Hu, R., 2022. Identification of critical nodes for the Integrated Energy Systems based on complex networks and unified energy flows. *Journal of Physics: Conference Series*, 2301(1), 012013. https://doi.org/10.1088/1742-6596/2301/1/012013

[41] Liu, S., Yin, X., Zhao, Y., 2021. Steady-State Modeling and Power Flow Calculation of Integrated Electric-Gas Coupling Energy System Based on Energy Circuit Theory. *International Conference on Life System Modeling and Simulation*, 30 October - 1 November, Suzhou, China, 55-63. https://doi.org/10.1007/978-981-16-7210-1_6

[42] Huang, B., Wang, L., Wang, R., 2022. A unified model for transient flow analysis of the integrated electric power and natural gas system with multiple time scales. *International Journal of Electrical Power & Energy Systems*, 142, 108133. https://doi.org/10.1016/j.ijepes.2022.108133

[43] Mi, J., Su, J., Xue, Y., 2026. Energy circuit theory-enabled quasi-dynamic security assessment for integrated electricity-gas energy system. *Energy Conversion and Management*, 363, 121673. https://doi.org/10.1016/j.enconman.2026.121673

[44] Ou, K., Ye, W., Zhang, X., 2025. An energy-circuit-based fuel cell air compressor system model reconstruction and predictive control approach. *Renewable Energy*, 254, 123696. https://doi.org/10.1016/j.renene.2025.123696

[45] Chen, B., Sun, H., 2020. Energy circuit theory of integrated energy system analysis (I): gaseous circuit. *Chinese Journal of Electrical Engineering*, 40(2), 436-443.

[46] Chen, B., Sun, H., 2020. Energy circuit theory of integrated energy system analysis (III): steady and dynamic energy flow calculation. *Chinese Journal of Electrical Engineering*, 40(15), 4820-4831.

[47] Goyal, S., Llop, M., 2024. The shipping industry under the EU Green Deal: An Input-Output impact analysis. *Transportation Research Part A: Policy and Practice*, 182, 104035. https://doi.org/10.1016/j.tra.2024.104035

[48] Li, Y., Yang, X., Du, E., 2024. A review on carbon emission accounting approaches for the electricity power industry. *Applied Energy*, 359, 122681. https://doi.org/10.1016/j.apenergy.2024.122681

[49] Ditl, P., Šulc, R., 2024. Calculations of $CO_2$ emission and combustion efficiency for various fuels. *Energy*, 290, 130044. https://doi.org/10.1016/j.energy.2023.130044

[50] Ghasemi, M., Trojovský, P., Trojovská, E., 2023. Gaussian bare-bones Levy circulatory system-based optimization for power flow in the presence of renewable units. *Engineering Science and Technology, an International Journal*, 47, 101551. https://doi.org/10.1016/j.jestch.2023.101551

[51] Liao, P., Wang, Z., Li, S., 2026. Time-frequency domain transformation dynamic hydrogen-electric energy network for efficient power coordination and economic scheduling in zero-emission ship power systems. *Energy*, 140521. https://doi.org/10.1016/j.energy.2026.140521

[52] Fang, S., Fang, Y., Wang, H., 2020. Optimal heterogeneous energy storage management for multienergy cruise ships. *IEEE Systems Journal*, 14(4), 4754-4764. https://doi.org/10.1109/JSYST.2020.2966711